Title

Simulation of wellbore construction in offshore unconsolidated methane hydrate-bearing formation

Authors

Sasaki, T
Soga, K
Elshafie, MZEB

Publication Date

2018-12-01

DOI

10.1016/j.jngse.2018.10.019

Peer reviewed

Title

Simulation of wellbore construction in offshore unconsolidated methane hydrate-bearing formation

Tsubasa Sasaki[a], Kenichi Soga[b], Mohammed Elshafie[c]

[a]Department of Engineering, University of Cambridge, Cambridge, CB2 1PZ, UK
[b]Civil and Environmental Engineering, University of California-Berkeley, Berkeley, CA, 94720, USA
[c]Department of Civil and Architectural Engineering, College of Engineering, Qatar University, P.O Box: 2713, Doha, Qatar

1. Introduction

The results from the recent field trials of methane gas production from the hydrate bearing sediments in the Mackenzie Delta in Canada (Yamamoto & Dallimore 2008) and in the Nankai Trough in Japan (Boswell 2013; Yamamoto et al. 2014) show that the adequate control of formation integrity during gas production is one of the main engineering challenges to achieve reliable gas production for commercial purposes. Offshore methane hydrate reservoirs are often located at shallow depths where the formation is still unconsolidated. Gas production from such soft formation has resulted in sand production during the Nankai Trough field trial (Yamamoto 2015). Sand production not only influences the gas production but also leads to the loss of formation lateral support, making the well vulnerable to buckling and collapse (Veeken et al. 1994; Shute et al. 2004).

During wellbore construction, the integrity of the unconsolidated formation near the wellbore could be altered, which in turn affects the interpretation of downhole tests. At the Nankai Trough site, mini-frac tests were conducted but the estimation of the minimum horizontal stress from the tests was found to be difficult (Matsuzawa et al. 2006; Yamamoto et al. 2005; Yamamoto et al. 2006). Figure 1 shows the estimated minimum horizontal stress values of the formation in the Nankai Trough. The symbols in the graph are the estimates from the mini-frac tests (closure pressure and propagation pressure) conducted at the A1-E1 well (Takahashi & Tsuji 2005) while the lines are the theoretical estimates calculated assuming the formation density of 1.75 g/cm^3 and seawater density of 1.027 g/cm^3 by Equation 1:

$$\sigma_h = K_0(\sigma_v - p) + p \quad (1)$$

where σ_h = horizontal total stress; σ_v = vertical total stress; p = pore fluid pressure; K_0 = ratio between the vertical and horizontal effective stresses (as in K_0 consolidation test). The figure shows that the estimated values of the minimum horizontal stress from the mini-frac tests are scattered over a wide range of horizontal stress levels and were not consistent with the estimates from a typical K_0 value of about 0.5 for normally consolidated soil.

Figure 2 shows the caliper measurement data of the A1-W well (Takahashi & Tsuji 2005), which was located about 50 m in the north from the A1-E1 well. The borehole radius is normalized by the radius of the drill bit. Considerable borehole enlargement was observed in the overburden and underburden layers of the unconsolidated Nankai Trough formation. This indicates that the formation was disturbed by the well construction process.

It is hypothesized in this study that well construction process has an impact on the formation integrity. The aim of this study is to evaluate the possible magnitude of such wellbore construction-induced disturbance. Since the direct evaluation of formation disturbance by wellbore construction process is difficult to perform in the field, numerical simulations with a calibrated formation constitutive model is employed in this study to assess the integrity of the formation. Despite its shallow depth compared to conventional oil and gas wells where the stress environment could be more severe, the stress disturbance in the Nankai Trough formation during well construction process could be significant due to the unconsolidated nature and highly nonlinear hydrate saturation profiles of the formation. Well construction in such formation should have unique consequences on the integrity of the formation, which could provide insights into successful well construction techniques for future explorations.

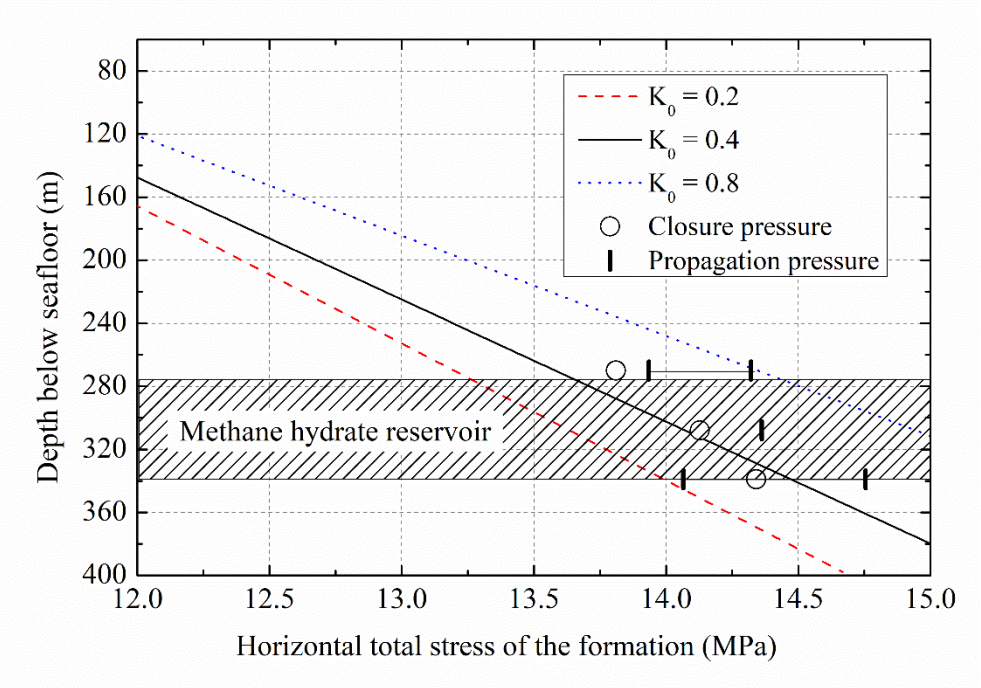

Figure 1 Estimated values of the minimum horizontal stress of the Nankai Trough formation.

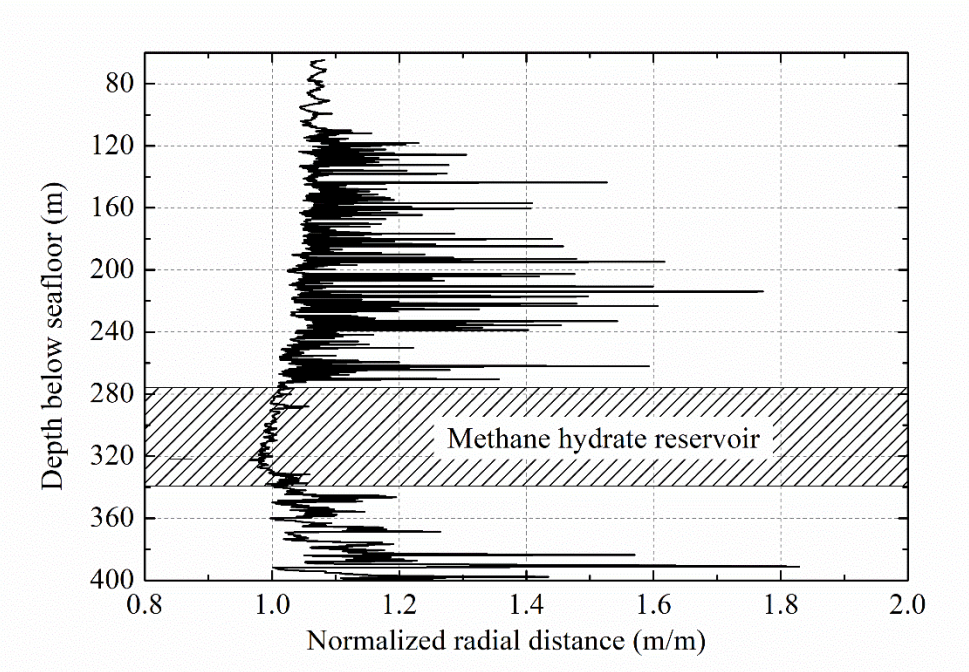

Figure 2 Borehole enlargement after the drilling of the Nankai Trough formation.

Different stages of wellbore construction affect the integrity of the wellbore. Bosma et al. (1999) conducted a finite element analysis to demonstrate that the integrity of wellbore would depend on the mechanical properties of the cement. Ravi et al. (2002) also emphasized the importance of cement integrity, which was found to be dependent on the formation properties. Gray et al. (2007) performed a three-dimensional finite element analysis of a wellbore construction to show that plastic deformation of the formation during wellbore construction would concentrate in the direction of the minimal horizontal stress. Oyarhossein & Dusseault (2015) investigated the debonding effect at the cement-formation interface. They found that, the stiffer the formation is, the more likely debonding at the cement-formation interface is going to happen. This is due to the inability of the stiff formation to follow the cement deformation during shrinkage.

Although the findings from the abovementioned numerical studies have contributed to the understanding of wellbore integrity, some important features of wellbore construction process and the behavior of the formation have yet to be considered. Firstly, the formation constitutive models (e.g., linear elastic-Mohr Coulomb plastic model) used in the past studies are too simple to simulate the complex mechanical behavior of the unconsolidated sediments at the Nankai Trough. Secondly, the model is often simplified to a plane-strain thin horizontal formation layer as the radial deformation would be the dominant deformation mechanism. Since the integrity of the formation would vary at different depths from the seafloor, a model with the whole wellbore depth needs to be constructed. Thirdly, formation excavation and cementing processes need to be explicitly modelled. The relative effect of different wellbore construction processes on the extent of formation disturbance is of interest in this study.

In the present study, a finite element analysis was carried out to assess the effect of wellbore construction on the integrity of the unconsolidated Nankai Trough formation in Japan. The main objectives are (i) to develop a modelling methodology of well construction process, (ii) to assess the zone and magnitude of well construction-induced disturbance in the formation and (iii) to evaluate relative impact of each well construction stage on the integrity of the formation. The geometry of the axi-symmetric model was based on that of an experimental wellbore (i.e., the A1-E1 well) constructed in 2004 in the Nankai Trough. The constitutive model for the formation incorporates the effect of methane hydrate on the formation mechanical properties, such as strength, stiffness, and dilation (Hyodo et al. 2014; Hyodo et al. 2013; Masui et al. 2005; Masui et al. 2007; Yoneda et al. 2015; Miyazaki et al. 2011). The methane hydrate critical state (MHCS) model proposed earlier by the authors (Uchida et al. 2012) was employed. The MHCS model is based on the Modified Cam-Clay model (Roscoe & Burland 1968) and it is capable of modelling the effect of methane hydrate on the formation mechanical properties. The MHCS model was

calibrated against the triaxial test data of the formation core samples recovered from the Nankai Trough (Yoneda et al. 2015; Nishio et al. 2011).

The simulated wellbore construction included the stages of drilling, casing hanging, cementing, cement hardening/shrinkage and casing landing. The cement volume shrinkage was varied between 0% and 0.75%, which are within a reasonable range of the cement employed for the Nankai Trough field trials (Sasaki et al. 2018).

2. Finite element modeling

2.1. Model geometry

A two-dimensional axi-symmetric finite element model was constructed. The model geometry was designed by Xu (2014) and it was based on the A1-E1 well drilled in 2004 at the Atsumi No.2 knoll in the Nankai Trough (Takahashi & Tsuji 2005). The A1-E1 well was constructed as part of the multi-well exploration program implemented in 2004 at the Nankai Trough and it was organized by Japan Oil, Gas and Metals National Corporation (JOGMEC). In total, 32 wells were drilled at 16 locations by the drill ship "JOIDES Resolution" over a 122-day period. The main objectives of the exploration program were (i) to assess suitable drilling technologies for future exploration and (ii) to obtain accurate temperature profiles of the formation.

Figure 3 shows the dimensions of the two-dimensional axi-symmetric model with the boundary conditions. The seafloor was 1,002 m below the sea surface and the depth of the well was 404 m from the seafloor. The depth of the formation in the model was set to 430 m from the seafloor. The methane hydrate-bearing interval (i.e., 277 m-339 m) was overlaid by a clayey layer (0 m-277 m) and was underlain by a sandy layer (i.e., 339 m-430 m). In order to avoid any boundary effects, the radial length of the formation was set to 50 m, which was greater than 200 times the radius of the 17 1/2-in. borehole for the conductor casing. The wellbore was comprised of a conductor casing (0 m-53 m) and a surface casing (0 m-404 m) with cement in the annuli. The outer diameter of the conductor was 0.340 m (13 3/8-in.) which was placed in a 0.445 m (17 1/2-in.) diameter borehole. The diameter of the surface casing was 0.244 m (9 5/8-in.) and it was placed in a 0.311 m (12 1/4-in.) diameter borehole. The wall thicknesses of the conductor and surface casing were 0.00965 m and 0.0100 m, respectively. A constant formation/water pressure boundary was applied on the outer radial boundary of the model.

A finite element code, Abaqus, was used for the simulations. The model was discretized into eight-node quadratic-displacement elements (casing and cement) and eight-node quadratic-

displacement bilinear-pore pressure elements (formation). In total, the model was discretized into 37,051 elements and 112,250 nodes. The spatially-varying mesh size of the elements (Figure 4) was designed by Xu (2014). The vertical mesh size of the methane hydrate-bearing interval was set to be finer (0.400 m) than that of the overburden and underburden layer (1.17 m). The radial mesh size of the formation was gradually varied from fine mesh near the symmetric axis (2.32 mm) to coarse mesh at the outer radial boundary of the model (4.72 m).

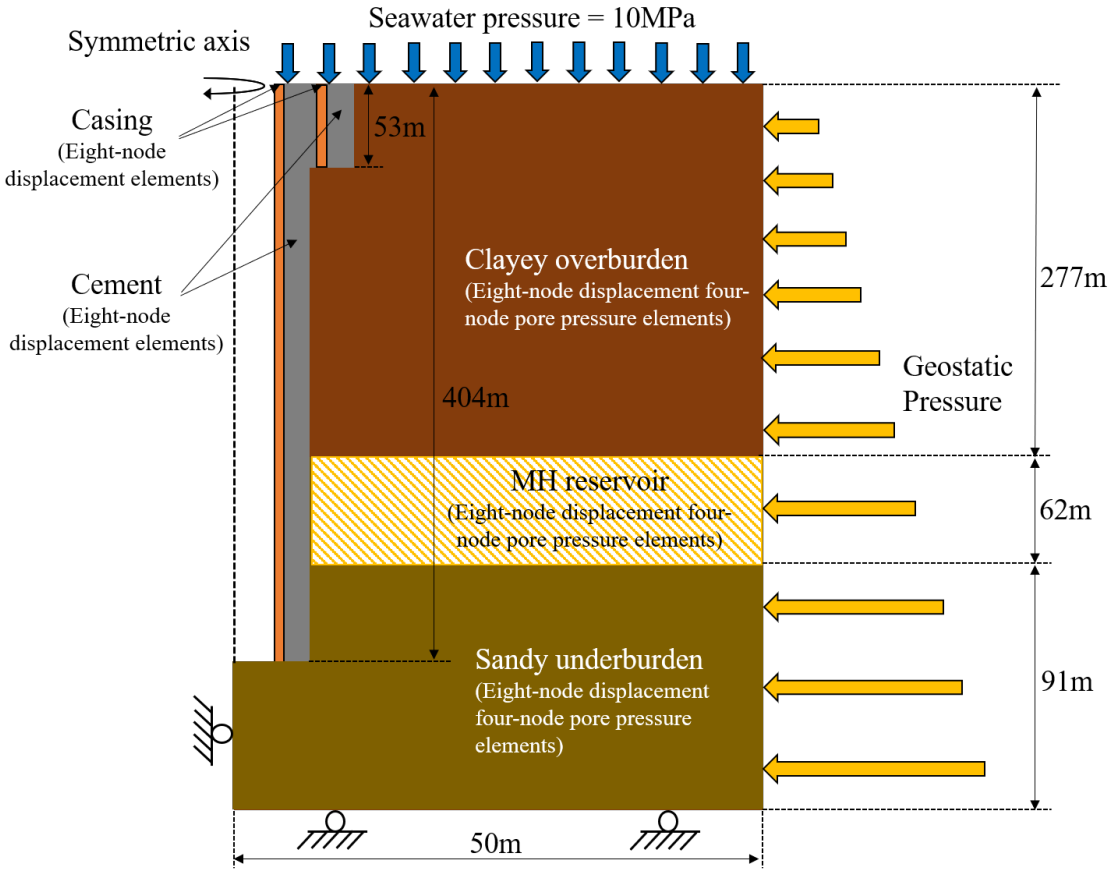

Figure 3 Geometry of the 2D axi-symmetric finite element model [after Xu (2014)].

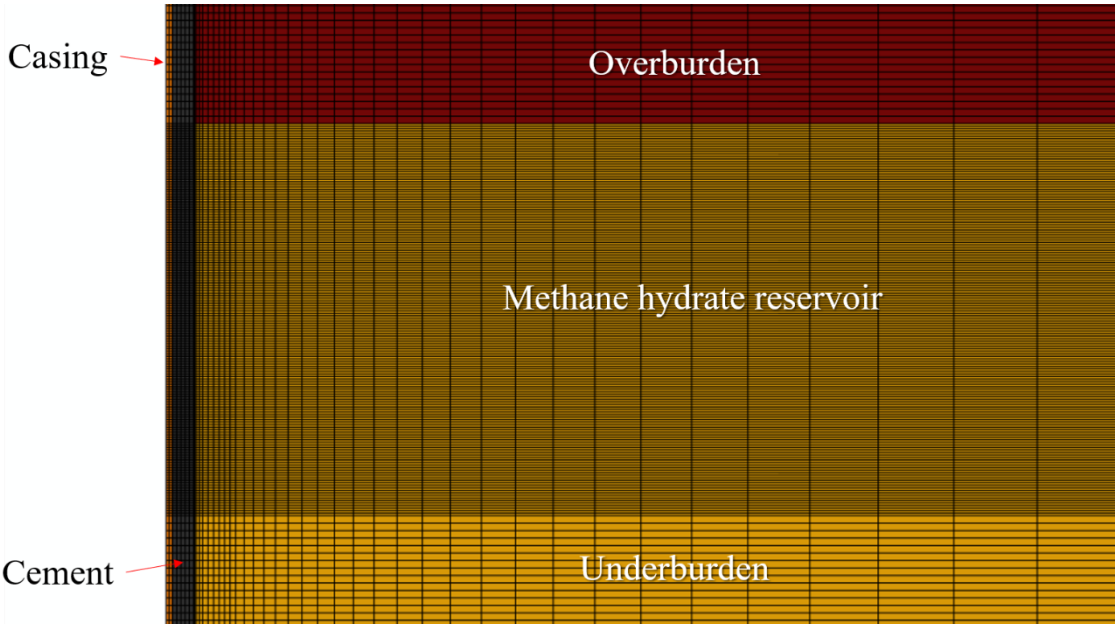

Figure 4 Mesh of the 2D axi-symmetric model around the wellbore and reservoir layer [after Xu (2014)].

2.2. Constitutive models

Methane hydrate critical state (MHCS) model (Uchida et al. 2012) was employed to simulate the behavior of the formation. The MHCS model is based on the Modified Cam-Clay model (Roscoe & Burland 1968) and it is capable of simulating the enhancement of stiffness, strength and dilation of the formation by the presence of methane hydrate (Miyazaki et al. 2007; Masui et al. 2007; Masui et al. 2005). The subloading surface (Hashiguchi 1989) is incorporated to facilitate a smooth transition from the elastic to plastic behavior. The model parameters of the MHCS model were calibrated against the triaxial test data on the core samples recovered from the Nankai Trough (Nishio et al. 2011; Yoneda et al. 2015). The calibration results are demonstrated in Figure 5 and Figure 6. The calibration error for the excess pore pressure of the clayey overburden (Figure 5b) at the depth of 115.2 m and 240.1 m seems relatively large at large axial strain levels. However, this might be due to the poor quality of the samples taken at depths below 40 m as Nishio et al. (2011) pointed out in his paper. The calibrated parameters for the clayey overburden layer, methane hydrate reservoir and sandy underburden layer are shown in Table 1. The density and void ratio of the formation were determined from the logging data given in Suzuki et al. (2015). The hydrate saturation and permeability distributions were also obtained from the logging data (Figure 7). Details of the MHCS model and its parameters are provided in the Appendix of this paper.

The casings and cement were assumed to be isotropic linear elastic materials. The Young's

modulus and Poisson's ratio of the casings are set to 200 GPa and 0.27, respectively. For the cement, the model parameters were varied with time during the hardening stage. The transition from slurry to hardened cement was modeled by linearly changing the Young's modulus and Poisson's ratio with time. The Young's modulus and Poisson's ratio for the slurry cement were 0.131 GPa and 0.49, while they were 3.81 GPa and 0.21 for the hardened state. The densities of the casing and cement were set to 8000 kg/m^3 and 1370 kg/m^3, respectively.

Table 1 Calibrated MHCS model parameters for the formation.

	Clayey overburden	Methane hydrate reservoir	Sandy underburden
Depth (m)	0~277	277~339	339~430
Saturated bulk density (kg/m^3)	1750	1750~2000	2000
Initial void ratio	1.31	1.31~0.717	0.717
Gradient of compression line, λ	0.18	0.10	0.10
Gradient of swelling line, κ	0.03	0.02	0.02
Critical state frictional constant, M	1.30	1.37	1.37
Poisson's ratio, ν	0.25	0.35	0.35
Subsurface constant, u	15	8	8
Stiffness enhancement constant, m_2	0	200	0
Hydrate degradation constant, m_1	0	2.0	0
Dilation enhancement constant, a	0	20	0
Dilation enhancement constant, b	0	1.4	0
Cohesion enhancement constant, c	0	0.5	0
Cohesion enhancement constant, d	0	1.4	0

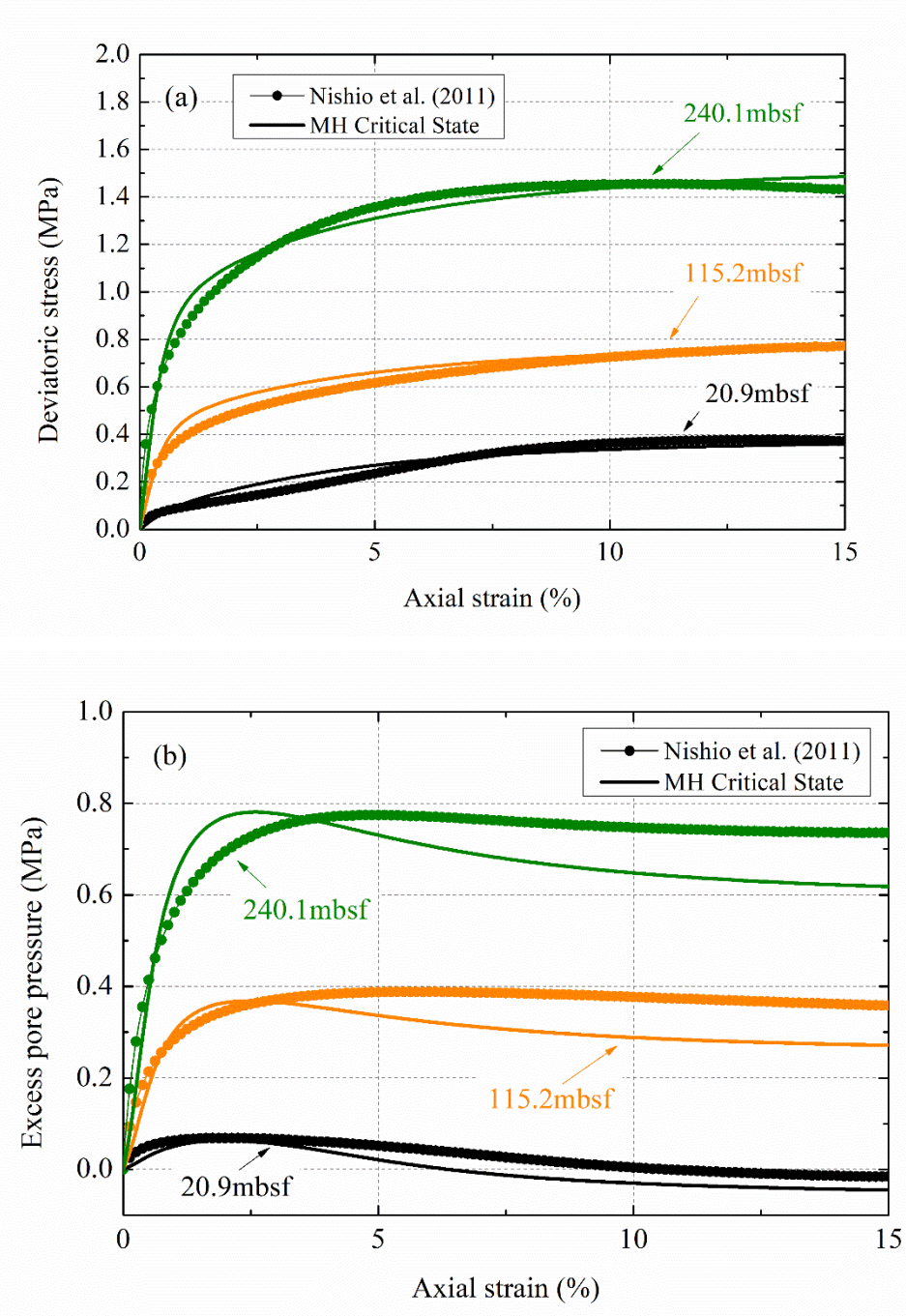

Figure 5: Calibration result of the MHCS model for the clayey overburden: (a) deviatoric stress vs. axial strain; (b) excess pore pressure vs. axial strain.

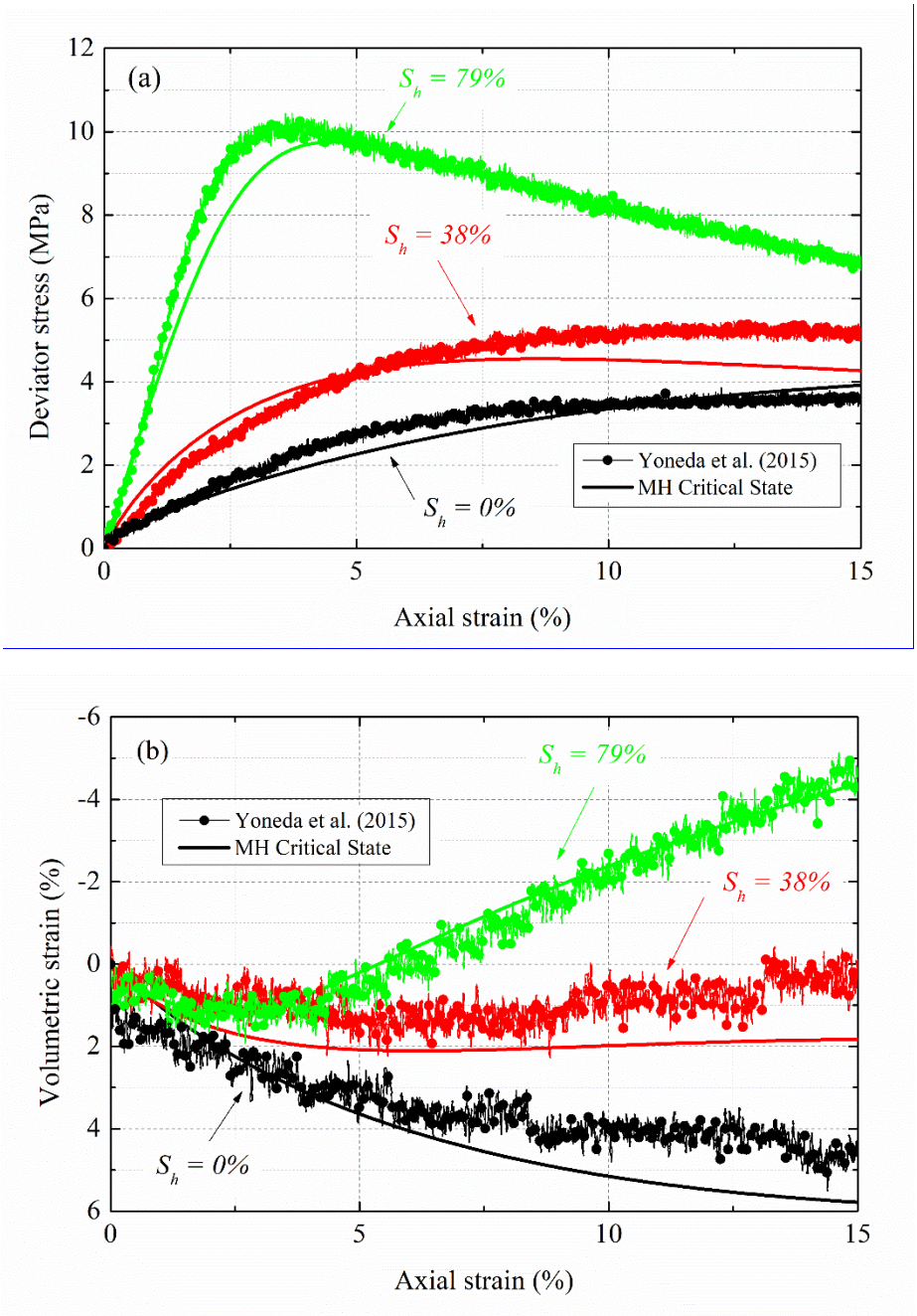

Figure 6: Calibration result of the MHCS model for the methane hydrate reservoir and sandy underburden: (a) deviatoric stress vs. axial strain;(b) volumetric strain vs. axial strain.

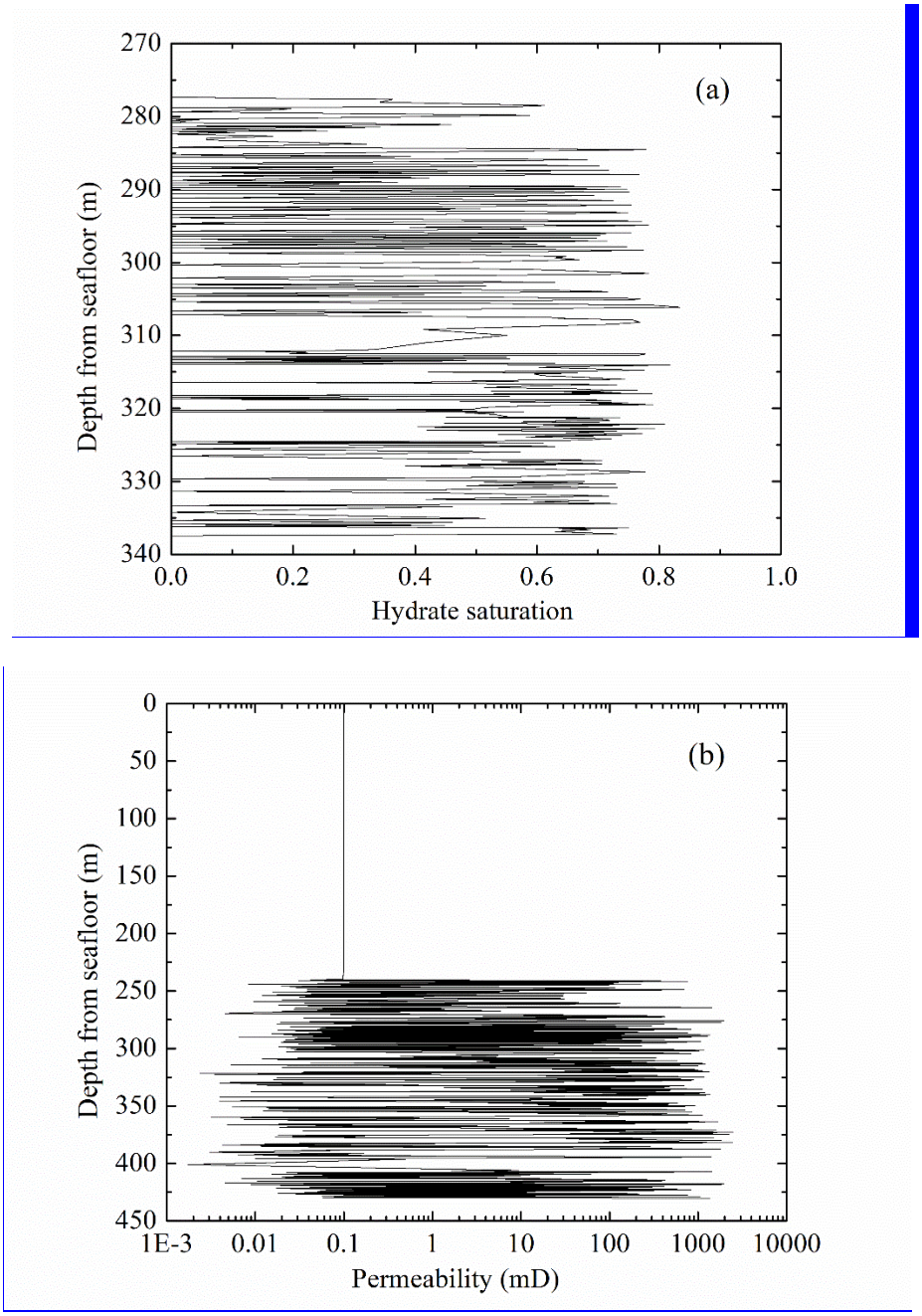

Figure 7: Distributions of (a) hydrate saturation and (b) permeability in the formation.

2.3. Construction processes of the wellbore

The construction process of the A1-E1 well was modelled in ten separate stages. The schematic diagrams of the construction stages are shown in Figure 8. Table 2 illustrates the modeled construction stages and their durations. It starts from (i) drilling, followed by (ii) casing hanging, (iii) cementing, (iv) cement hardening/shrinkage and finishes with (v) casing landing. These five stages were applied first for the conductor casing placement and then repeated for the surface

casing placement. It is noted that hydrate dissociation or reformation was not simulated in this study as the pressure and temperature conditions of the A1-E1 well was maintained during well construction process by using in situ seawater as drilling fluid. Also, any thermal stress development in the formation was not considered for the same reason. The details of each construction stage are described below.

Table 2 The modeled construction stages.

	Construction activity	Duration (hour)
1.	Drilling (17 1/2-in.)	14.4
2.	Casing hanging (13 3/8-in.)	Immediate
3.	Cementing	Immediate
4.	Cement hardening/shrinkage	40.8
5.	Casing landing (13 3/8-in.)	Immediate
6.	Drilling (12 1/4-in.)	30.2
7.	Casing hanging (9 5/8-in.)	Immediate
8.	Cementing	Immediate
9.	Cement hardening/shrinkage	40.8
10.	Casing landing (9 5/8-in.)	Immediate

(i) Drilling

The drilling process was modelled by removing the formation elements located inside the borehole. Upon the removal of the elements, the forces on the nodes of the neighboring elements along the borehole were linearly decreased with time from the values before the element removal to zero. The hydrostatic pore fluid pressure boundary condition was specified on the nodes of the borehole surface to model the drilling with seawater, which was actually performed for the A1-E1 well. Also, hydrostatic surface pressure boundary condition was implemented on the surface of the borehole. Figure 8a shows the modelling process of the drilling stage.

The load due to weight on bit (WOB) at the bottom of the borehole was not considered in this study by assuming that WOB was not significant during the drilling of the unconsolidated formation. This assumption could be validated by the speed of drilling which was 197 ft/h (60 m/h) for the overburden and underburden layer and 66 ft/h (20 m/h) for the methane hydrate-bearing layer (Takahashi & Tsuji 2005). Such a high drilling speed indicates the ease of drilling the unconsolidated formation. Also, the nozzle hydraulic jet during drilling and potential shaft friction between the drilling string and borehole wall were not considered. Thus, results of the simulation would indicate a lower-bound estimate for the disturbance of the formation during

drilling.

(ii) Casing hanging

The casing elements, which had been deactivated at the start of the simulation, were activated in this stage. Zero vertical displacement boundary condition was enforced at the top nodes of the casing to simulate the hanging operation. Hydrostatic surface pressure boundary condition was applied on the surface of the casing. The hydrostatic surface pressure and pore pressure boundary condition on the borehole surface and nodes were maintained in this stage. The details of the casing hanging stage are illustrated in Figure 8b.

(iii) Cementing

To simulate the cementing stage, the hydrostatic surface pressure boundary condition on the casing outer surface and borehole surface was replaced by a new surface pressure boundary condition whose magnitude corresponded to the density of the cement slurry. The density of cement slurry employed for the A1-E1 well was 1370 kg/m^3 (Takahashi & Tsuji 2005). The hydrostatic surface pressure boundary condition was maintained on the inner surface of the casing to simulate the pressure from the drilling fluid (i.e., seawater), whereas the hydrostatic pore pressure boundary condition on the borehole surface was removed (i.e., pore pressure boundary condition was left unspecified). Figure 8c depicts the boundary conditions of the cementing stage.

(iv) Cement hardening and shrinkage

The cement elements, which had been deactivated at the start of the simulation, were activated in the annulus and the surface interaction with the casing and formation were initiated. All the surface pressure boundary conditions in the wellbore were removed except for the hydrostatic surface pressure boundary condition on the inner surface of the casing.

To simulate cement hardening, the values of Young's modulus and Poisson's ratio were linearly varied with time from those of the slurry (0.131 GPa and 0.49) to those of the hardened cement (3.81 GPa and 0.21). In addition, the interface friction angle was linearly increased from 0^o to 30^o, which is an average friction angle of the cement interface to the casing and soil (Kakumoto et al. 2012; Yoneda et al. 2014). The interface friction stress was computed by the Coulomb friction model. To model cement shrinkage, the volume of the cement was linearly decreased with time through fictitious thermal contraction. Due to the simultaneous development of the cement interface friction and shrinkage, the compressive vertical stress in the cement decreases as the cement column was restrained from displacing downward.

The interface pressure was calculated by the penalty method with an augmentation iteration scheme (i.e., augmented Lagrange method). In this method, contact pressure is calculated by multiplying surface penetration distance by the stiffness of representative underlining elements. The contact pressure is then augmented through an iterative scheme to reduce the surface penetration below a limit value, which is based on a characteristic element length of the finite element model. Surface separation was allowed (i.e., zero contact stiffness in tension) even though surface separation never occurred in the simulation due to high initial contact pressure. Figure 8d shows the details of the cement hardening/shrinkage stage.

It is noted that the generation of cement hydration heat and resultant heat conduction was not simulated in this study. If the temperature increase due to cement hydration heat was large, methane hydrate would dissociate and the integrity of the formation would be affected. However, a cement hydration analysis in a well annulus at the Nankai Trough (Sasaki et al. 2018) shows that the temperature increase due to cement hydration heat would be less than 0.5 °C. As a result, the assumption of negligible cement hydration heat and no hydrate dissociation is valid for this study.

(v) Casing landing

The zero vertical displacement boundary condition at the top nodes of the casing was removed in this stage to release the casing from hanging. The hydrostatic surface pressure boundary condition on the inner surface of the casing was maintained. These procedures are illustrated in Figure 8e.

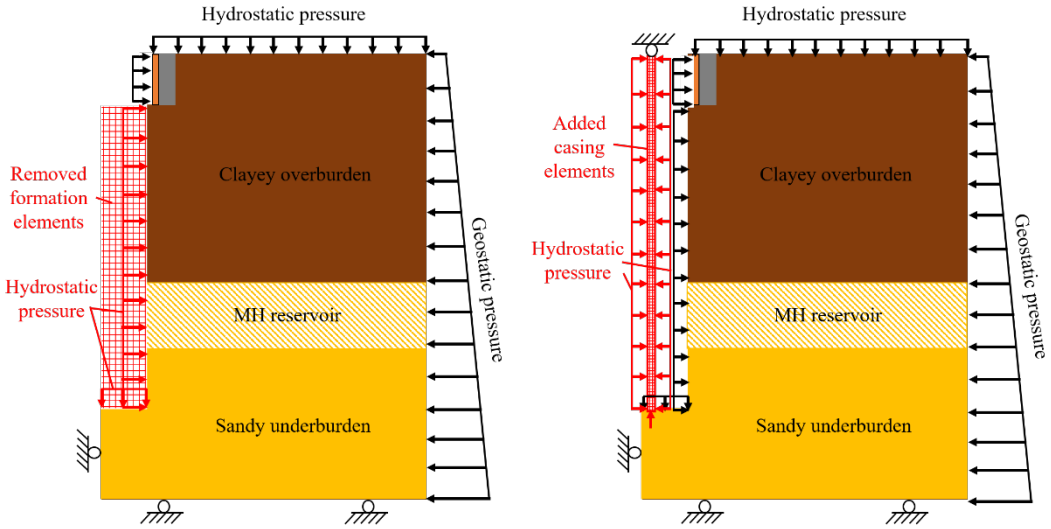

(a) (b)

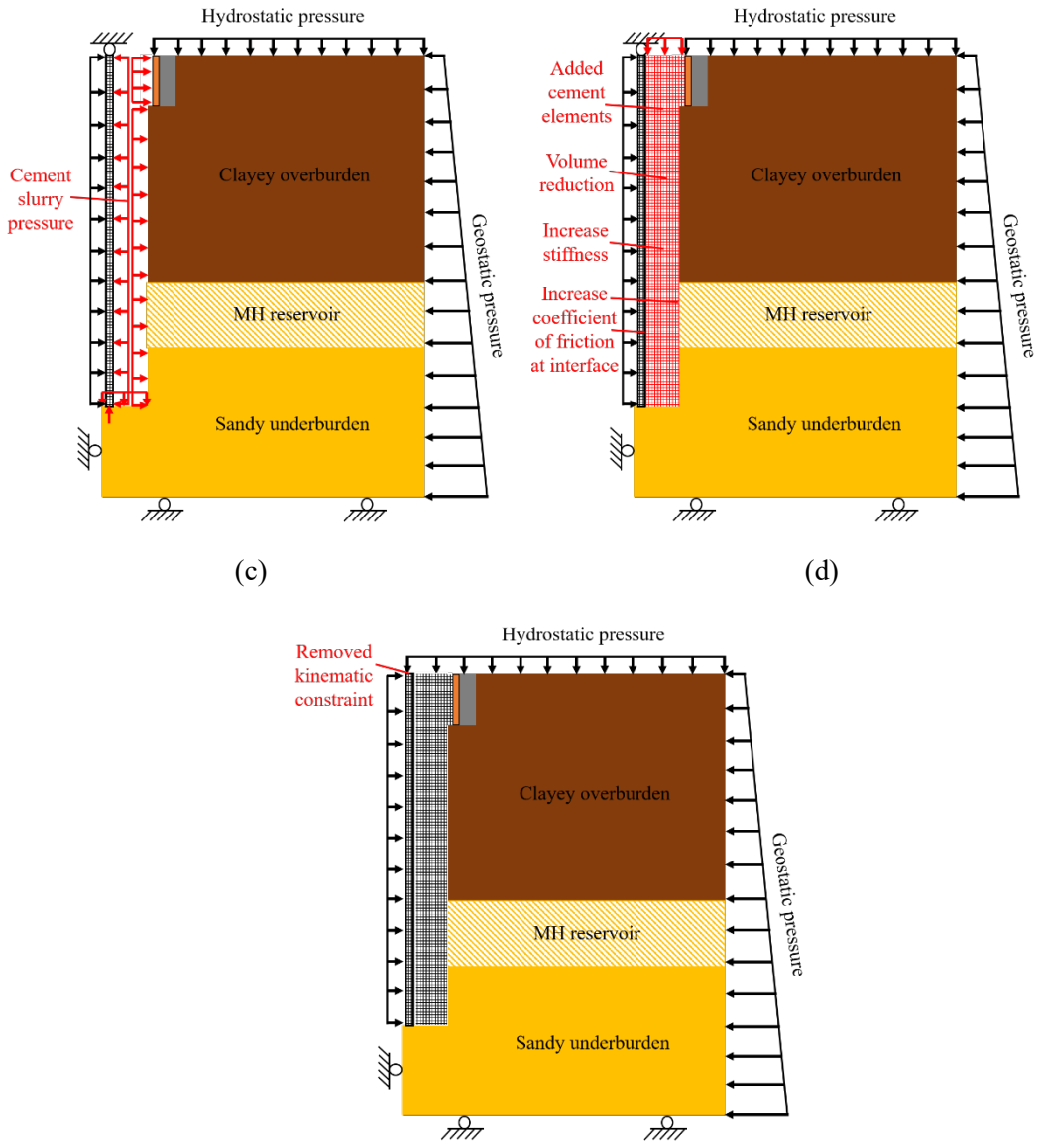

Figure 8 The simulated construction processes of wellbore: (a) drilling; (b) casing hanging; (c) cementing; (d) cement hardening/shrinkage; (e) casing landing.

2.4. Cement volume shrinkage

Cement volume shrinkage occurs due to cement hydration process. The volumes of cement shrinkage reported in the literature varies from 0.1% to 4.5% (Goboncan & Dillenbeck 2003; Backe et al. 1998; Justnes et al. 1995; Chenevert & Shrestha 1991; Chenevert & Shrestha 1987). This large variance is not only because the cement volume shrinkage is significantly affected by the temperature and pressure conditions and the employed test method (Reddy et al. 2009), but also because the reported values often include shrinkage before the initial set of cement (i.e.,

shrinkage within the thickening time). In actual cementing operations, shrinkage before the initial set is usually compensated by the drop of slurry column in the annulus (Thiercelin et al. 1998; Backe et al. 1999). On the other hand, shrinkage after the initial set cannot be compensated in the same way due to the development of friction and cohesion at the cement interface to casing and formation (Chenevert & Jin 1989). Therefore, shrinkage after the initial set is the relevant parameter for the simulation. Also, due to the vertical frictional resistance, shrinkage after the initial set occurs predominantly in the radial direction (Zhou & Wojtanowicz 2000).

The shrinkage volume of a typical oil well cement after the initial set is smaller than 1% according to the laboratory cement shrinkage experiments (Reddy et al. 2009; Appleby & Wilson 1996). However, cement shrinkage in laboratory conditions may differ from that in downhole conditions where the cement is surrounded by casing and formation. A numerical simulation on cement shrinkage in the downhole condition at the Nankai Trough was conducted by Sasaki et al. (2018) and they found that the shrinkage volume of cement employed at the Nankai Trough could reach up to 0.75%. Therefore, the shrinkage volume was varied between 0 to 0.75% in the simulation.

2.5. Initial horizontal stress of the formation

The initial horizontal stress of the formation was calculated through the lateral earth pressure coefficient, K_0 as shown in Equation 2:

$$\sigma'_h = K_0 \sigma'_v \tag{2}$$

where K_0 = lateral earth pressure coefficient; σ'_h = horizontal effective stress; σ'_v = vertical effective stress.

The effective stress in the equation refers to the Terzaghi effective stress, which is the total stress subtracted by pore fluid pressure ($\sigma' = \sigma - p$). Three different formulations for K_0 were used in this study. Equation 3 is the one frequently employed in the field of soil mechanics. This formulation takes into account the stress history of the formation on the current horizontal stress. The over-consolidation ratio (OCR) was calculated by dividing the maximum vertical effective stress experienced by the formation in the past by the current vertical effective stress. The past maximum vertical effective stress was estimated from the triaxial test data (Nishio et al. 2011; Yoneda et al. 2015) whereas the current vertical effective stress was obtained from the density data of the formation (Suzuki et al. 2015).

$$K_0 = (1 - \sin\phi')\mathrm{OCR}^{\sin\phi'} \tag{3}$$

where ϕ' = internal friction angle of the formation; OCR = overconsolidation ratio, i.e., the ratio of the past maximum vertical effective stress to the current vertical effective stress.

Equation 4 is another formula for K_0 which is often employed in the field of rock mechanics. It calculates K_0 assuming that the formation is an elastic material.

$$K_0 = \frac{\nu}{1-\nu} \tag{4}$$

where ν = Poisson's ratio of the formation.

A series of mini-frac test was performed at the Nankai Trough to estimate the minimum horizontal stress of the formation (Yamamoto et al. 2006; Yamamoto et al. 2005). The result suggested K_0 = 0.40 at 310 m below seafloor, which is approaching to the active pressure coefficient of the formation (K_a = (1-sinϕ')/(1+sinϕ')). It was also found through the anelastic strain recovery method that the difference between the maximum and minimum horizontal stress magnitudes would be small (Nagano et al. 2015). Accordingly, K_0 = 0.40 was also employed to calculate the initial horizontal stress of the formation. The three different K_0 profiles employed in this study are compared in Figure 9.

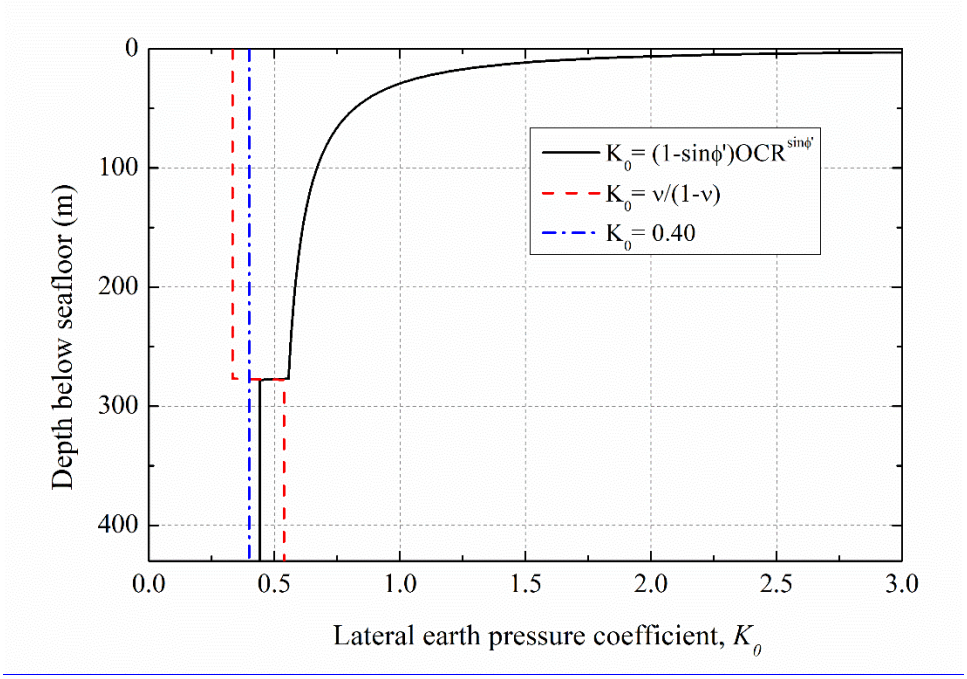

Figure 9 Three different distributions of the lateral earth pressure coefficient, K_0, employed to calculate the initial horizontal stress of the formation.

2.6. Initial conditions

The initial vertical effective stress was calculated based on the density distribution of the formation in the Nankai Trough (Suzuki et al. 2015). The initial horizontal effective stresses were assumed to have identical magnitudes. This assumption is considered to be valid for the formation in the Nankai Trough based on the anelastic strain recovery analysis on core samples (Nagano et al. 2015). The hydrostatic pore pressure was assigned as the initial pore pressure, which was calculated from the seawater density of 1027 kg/m^3. The initial porosities of the formation were determined from the in situ logging data (Suzuki et al. 2015).

2.7. Numerical solution scheme of the analysis

The simulation was performed by applying external load, which was induced by well construction process, as boundary conditions on the wellbore region of the model. In response to the input external load, displacement was calculated. Stress and strain were then calculated from the displacement through the constitutive model. Finally, internal load was calculated from the stress, which was then compared with the applied external load.

The solution was obtained iteratively by employing Newton's method. The convergence was considered to be satisfied if the load residual (i.e., difference between the external and internal

load) at the end of an iteration in an increment was smaller than 0.5% of the time- and spatially-averaged load of the entire model. If the load residual was greater than the tolerance value, another iteration was performed until the load residual was decreased below the tolerance value at all nodes in all degrees of freedom. In addition to the load convergence criterion, a displacement convergence criterion was specified such that the displacement calculated in the latest iteration (i.e., displacement correction) must be smaller than 1% of the total displacement calculated for the increment.

If the behavior of the model was found to be unstable due to material softening and/or buckling (i.e., negative stiffness), volume-proportional damping was applied to stabilize the model and to find a converged solution. The values of the damping factor were chosen in such a way that the incremental dissipated energy due to damping in an increment was smaller than 0.02% of the total strain energy of the model. Also, the cumulative dissipated energy due to damping was enforced to be smaller than 5% of the total strain energy of the model to make sure that the accuracy of the solution was not compromised due to damping.

3. Results and discussion

3.1. Effective stress and plastic strain in the formation during wellbore construction

The effective stresses, pore pressure and plastic deviatoric strain in the formation generated during the wellbore construction stages along the 12 1/4-in. dimeter borehole are presented in Figure 10. Positive effective stresses indicate compression using the traditional soil mechanics convention. The cement volume shrinkage was set to 0.75% while the initial horizontal stress of the formation was calculated with $K_0 = (1\text{-}\sin\phi')\mathrm{OCR}^{\sin\phi'}$.

The formation behavior during wellbore construction was dictated by the cavity contraction/expansion mechanism around the wellbore, i.e., an increase in the radial effective stress is accompanied by a decrease in the circumferential effective stress, and vice versa. During the drilling stage, the radial effective stress at the wellbore surface decreased to zero (Figure 10b) because pore pressure and surface pressure are equal to each other at the hydrostatic pressure along the borehole, simulating the drilling with seawater as the drilling fluid. In the meantime, the circumferential effective stress increased according to the cavity contraction mechanism. The vertical effective stress decreased because the formation developed plastic strain during the drilling stage, causing stress redistribution around the wellbore.

During the cementing stage, the borehole was enlarged because the pressure of the cement slurry

was greater than that of seawater. As a result, the cavity expansion mechanism occurred. The radial effective stress increased while the circumferential effective stress decreased. The vertical effective stress did not change significantly, which were consistent with the insignificant additional plastic strain development during this stage (Figure 10e).

During the cement hardening/shrinkage stage, the borehole contracted as the cement shrank in the radial direction, which rendered the formation to behave in the cavity contraction mechanism. At 0.75% shrinkage, the inward radial displacement of the borehole wall was calculated less than 1mm. Even at such small displacement the change in the radial and circumferential effective stress was approximately 0.2 MPa in the overburden/underburden and up to 1 MPa in the hydrate-bearing layer.

During the casing landing stage, the stresses along the borehole surface did not change substantially because the weight of the casing was primarily supported at the bottom of the borehole.

The pore pressure did not change significantly throughout the whole wellbore construction stages, even though small excess pore pressure was generated during the cementing stage. The majority of the plastic deviatoric strain was developed during the drilling stage, whereas the cement shrinkage stage developed minor additional plastic deformation. The oscillatory responses in the depths between 277 m and 339 m were due to steep changes in the formation mechanical properties arising from the highly heterogeneous distribution of hydrate saturation as shown in Figure 7a. Due to the bonding effect of methane hydrate, the formation in this interval can sustain tensile stress.

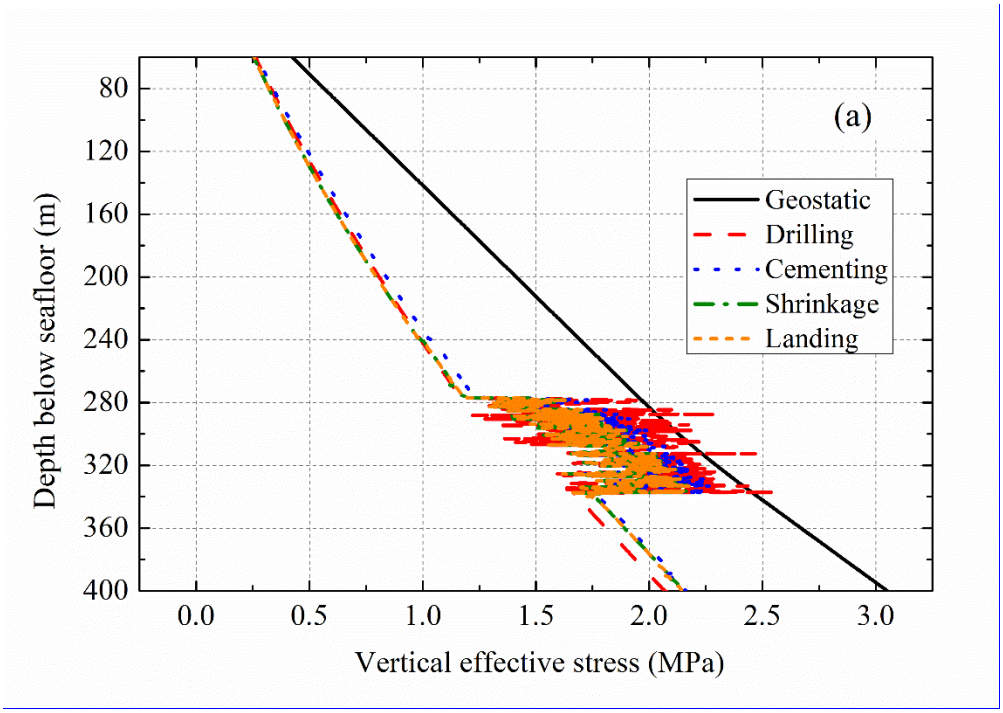
(a)
Depth below seafloor (m)
80
120
160
200
240
280
320
360
400
0.0
0.5
1.0
1.5
2.0
2.5
3.0
Vertical effective stress (MPa)
Geostatic
Drilling
Cementing
Shrinkage
Landing

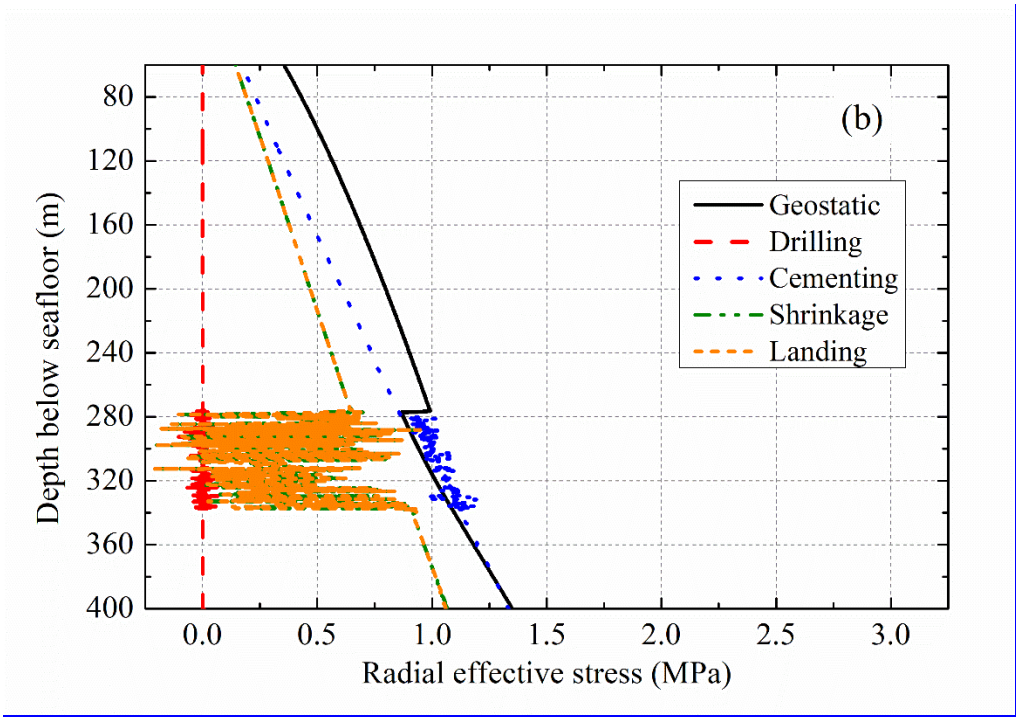
(b)
Depth below seafloor (m)
80
120
160
200
240
280
320
360
400
0.0
0.5
1.0
1.5
2.0
2.5
3.0
Radial effective stress (MPa)
Geostatic
Drilling
Cementing
Shrinkage
Landing

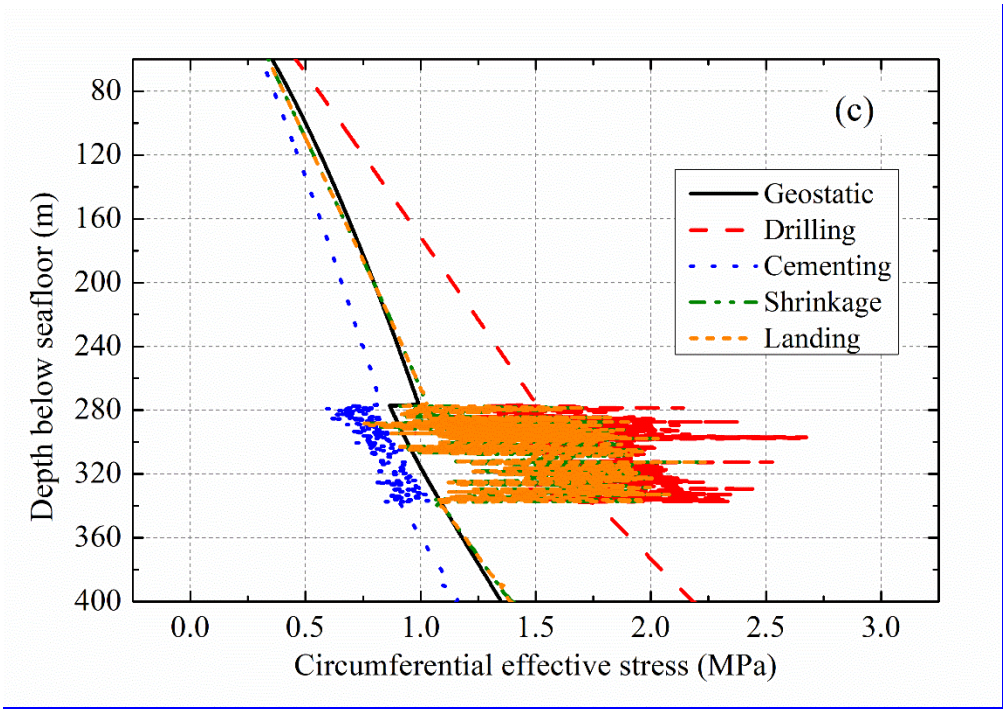
(c)
Geostatic
Drilling
Cementing
Shrinkage
Landing
Depth below seafloor (m)
80
120
160
200
240
280
320
360
400
0.0
0.5
1.0
1.5
2.0
2.5
3.0
Circumferential effective stress (MPa)

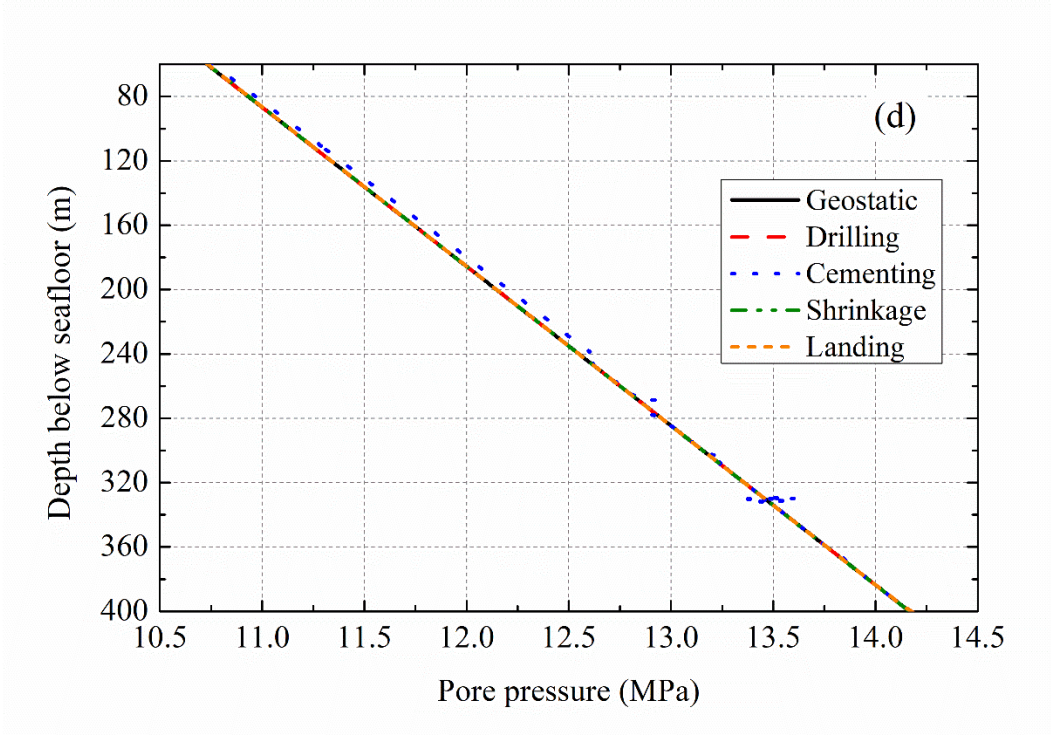
(d)
Geostatic
Drilling
Cementing
Shrinkage
Landing
Depth below seafloor (m)
80
120
160
200
240
280
320
360
400
10.5
11.0
11.5
12.0
12.5
13.0
13.5
14.0
14.5
Pore pressure (MPa)

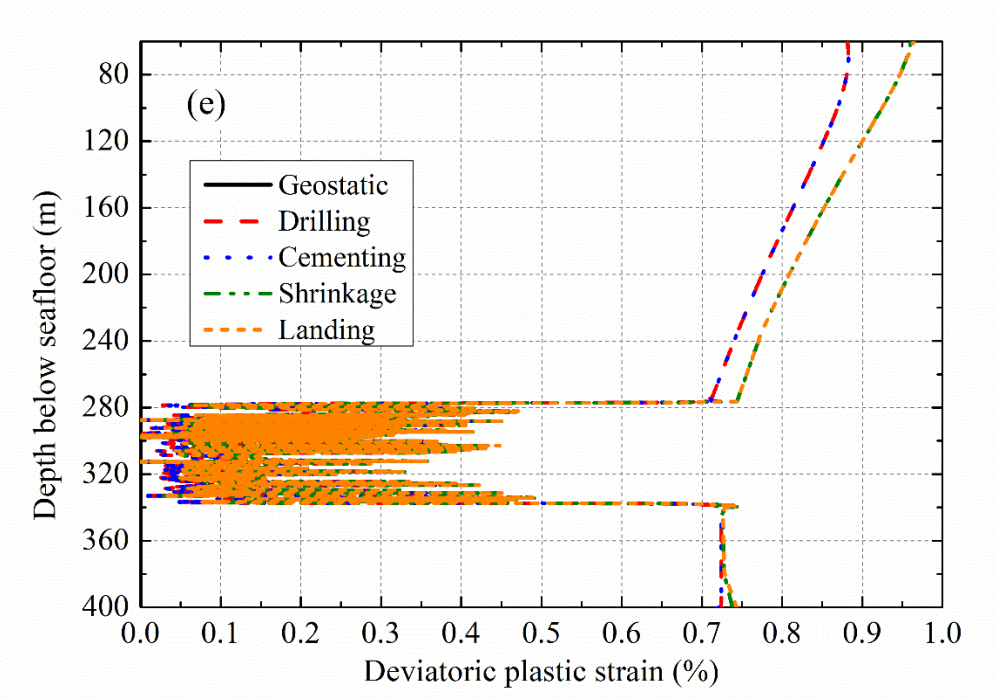

Figure 10: Behaviors of the formation along the 12 1/4-in. diameter borehole at each construction stage: (a) vertical effective stress; (b) radial effective stress; (c) circumferential effective stress; (d) pore pressure; (e) deviatoric plastic strain.

3.2. Zone of stress disturbance in the formation

Figure 11 show the effective stress contours at the end of wellbore construction near the 12 1/4-in. diameter borehole computed with different cement shrinkage volumes and initial horizontal stresses. The horizontal axes are denoted by the normalized radial distance, which was calculated by dividing the radius from the axi-symmetric axis by the radius of the 12 1/4-in. diameter borehole. For example, the normalized radial distance of seven corresponds to 1.09 m or 42.9 in. from the center of the wellbore.

Figure 11a-1 and a-2 show the effective stress contours with the cement shrinkage of 0% and 0.75%, respectively, with the initial horizontal stress calculated by $K_0 = (1\text{-}\sin\phi')\mathrm{OCR}^{\sin\phi'}$. Although the vertical effective stress recovered to the geostatic levels within the normalized radial distance of two, the disturbance to the radial and circumferential stresses propagated much further. With the cement shrinkage of 0%, the horizontal stresses were affected up to the normalized radial distance of three. In the clayey overburden layer, the radial effective stress around the borehole decreased while the circumferential effective stress increased with respect to their geostatic levels. The decrease in the circumferential effective stress near the borehole was due to the development of plastic strain which caused stress relaxation of the formation.

When the cement shrinkage was set to 0.75%, the zone of horizontal stress disturbance did not change at the normalized radial distance of three but the magnitudes increased. The stress disturbance in the reservoir and sandy underburden layer was less pronounced than that in the clayey overburden layer. This was because in these layers the initial horizontal stress levels were similar to the cement slurry pressure levels, which recovered to the geostatic stress levels during the cementing stage after they were disturbed by the drilling. Also, the spiky stress response in the methane hydrate reservoir (i.e., 277 m to 339 m) became apparent during the cement shrinkage stage. This is because the sublayers with low hydrate saturation accumulated greater plastic strain than those with high hydrate saturation during drilling and cementing, which in turn caused the former to become softer and the latter to maintain its stiffness. During the cavity contraction associated with cement shrinkage, the stiffness contrast of different layers turned into stress variation within the hydrate bearing layer, as illustrated in Figure 12a and b.

Figure 11b-1 and b-2 show the effective stress contours with the initial horizontal stress calculated by $K_0 = \nu/(1-\nu)$, and with the cement shrinkage of 0% and 0.75%, respectively. Both the area and the magnitude of the vertical effective stress decrease in the clayey overburden layer were smaller than those calculated in the case of $K_0 = (1-\sin\phi')\mathrm{OCR}^{\sin\phi'}$. This was because the initial horizontal stresses calculated by $K_0 = \nu/(1-\nu)$ were smaller than those by $K_0 = (1-\sin\phi')\mathrm{OCR}^{\sin\phi'}$, resulting in smaller stress changes and hence less plastic deformation during drilling. In fact, in the reservoir and sandy underburden layer where $K_0 = \nu/(1-\nu)$ resulted in larger initial horizontal stress than $K_0 = (1-\sin\phi')\mathrm{OCR}^{\sin\phi'}$, the area and magnitude of the vertical effective stress decrease were greater. The disturbance in the radial and circumferential effective stresses was also affected by the initial horizontal stress. When the initial horizontal stresses in the overburden layer were calculated by $K_0 = (1-\sin\phi')\mathrm{OCR}^{\sin\phi'}$, the radial effective stress decreased while the circumferential effective stress increased from their geostatic levels. When $K_0 = \nu/(1-\nu)$ was employed, the opposite response was obtained, i.e., the radial effective stress increased while the circumferential effective stress decreased around the borehole. This was because the initial horizontal stresses calculated by $K_0 = (1-\sin\phi')\mathrm{OCR}^{\sin\phi'}$were greater than the cement slurry pressure while those by $K_0 = \nu/(1-\nu)$ were smaller. As to the effect of cement shrinkage, the case of cement shrinkage of 0.75% reduced the stress disturbance in the overburden layer compared to that of 0%. The spiky stress response in the methane hydrate layer occurred as was the case with $K_0 = (1-\sin\phi')\mathrm{OCR}^{\sin\phi'}$.

Figure 11c-1 and c-2 show the cases where the initial horizontal stresses were calculated by $K_0 = 0.40$ with the cement shrinkage of 0% and 0.75%, respectively. The area and the magnitude of the vertical effective stress decrease were comparable to the other two cases, while the disturbance in

the radial and circumferential effective stresses was smaller. This was because the initial horizontal stresses calculated by K_0 = 0.40 were close to the cement slurry pressure. The horizontal stresses disturbed in the drilling stage was recovered to the geostatic levels in the cementing stage. In the methane hydrate layer, the horizontal stresses were significantly disturbed as was the case for the other initial horizontal stress cases.

Figure 12 and Figure 13 show the deviator stress-strain changes and deviator stress-mean effective stress changes (i.e., stress paths) of formation elements close to the wellbore during well construction for the case of K_0 = 0.4 and cement shrinkage volume = 0.75%. The following four elements were selected: (i) methane hydrate reservoir with low hydrate saturation (S_h = 1.0%), (ii) methane hydrate reservoir with high hydrate saturation (S_h = 78.3%), (iii) underburden sand layer and (iv) overburden clay layer.

In general, the horizontal stress disturbance in the methane hydrate layer was affected more by the cement shrinkage stage than by the other wellbore construction stages. The methane hydrate layers with high hydrate saturation (Figure 12b) exhibited stiffer response than those with low hydrate saturation (Figure 12a) during the cement shrinkage stage. The deviator stress magnitude in the high hydrate saturation layer after cement shrinkage increased to a comparable level to that achieved after the drilling. The stress paths in the high hydrate saturation layer (Figure 13a) showed negligible plastic strain development while in the low saturation layer some plastic strains accumulated as the stress state approached the yield surface (Figure 13b). The R value shown in Figure 13 indicates the ratio of the current stress to the yield stress. The small R values in the high methane hydrate saturation layer correspond to the stiff, elastic response of this layer mentioned earlier. The stress paths also show that the maximum stress ratios (i.e., q/p'), which occurred at the drilling stage, were 1.55 in the high hydrate saturation layer and 1.50 in the other layers. The pore pressure change was negligible at a level of few tens of kilopascal during the entire well construction stages. The shear resistance in the methane hydrate reservoir was concentrated in the layers with high hydrate saturation within the region of the normalized radial distance of three, i.e. 0.467 m or 18.4 in. from the center of the wellbore. The deviatoric stress-strain change and stress path in the overburden layer (Figure 12d and Figure 13d) and underburden layer (Figure 12c and Figure 13c) were similar to those in the low hydrate saturation layers in the reservoir. In these layers, significant plastic strain development was observed due to lack of reinforcement effect of methane hydrate.

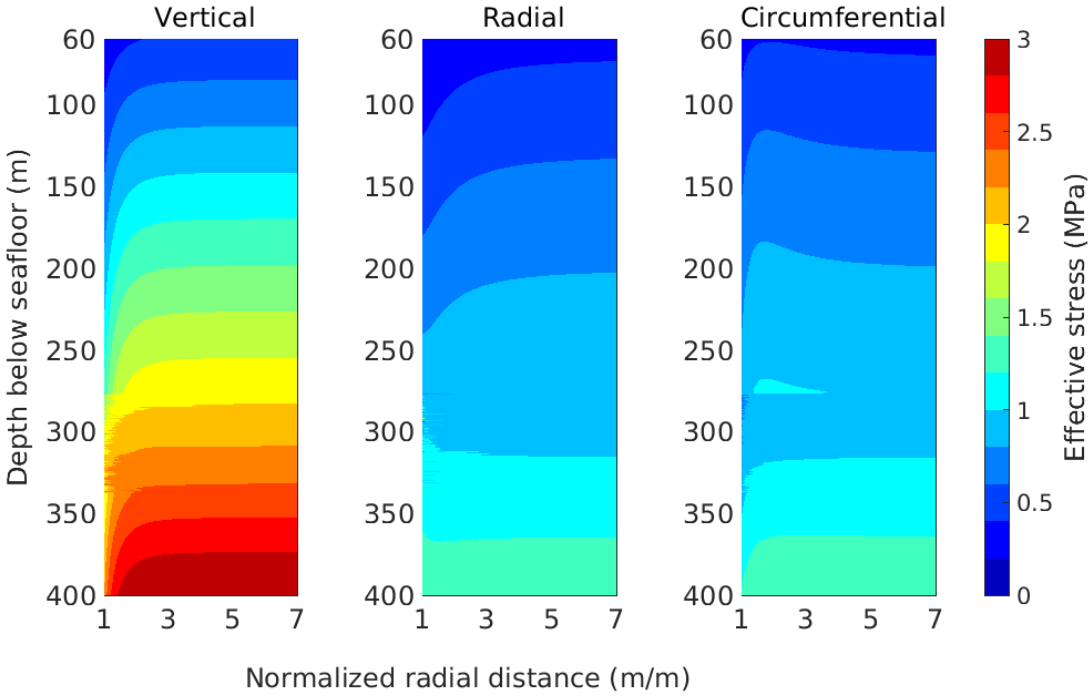
Vertical
Radial
Circumferential
Depth below seafloor (m)
60
100
150
200
250
300
350
400
1
3
5
7
Normalized radial distance (m/m)
Effective stress (MPa)
0
0.5
1
1.5
2
2.5
3

(a-1)

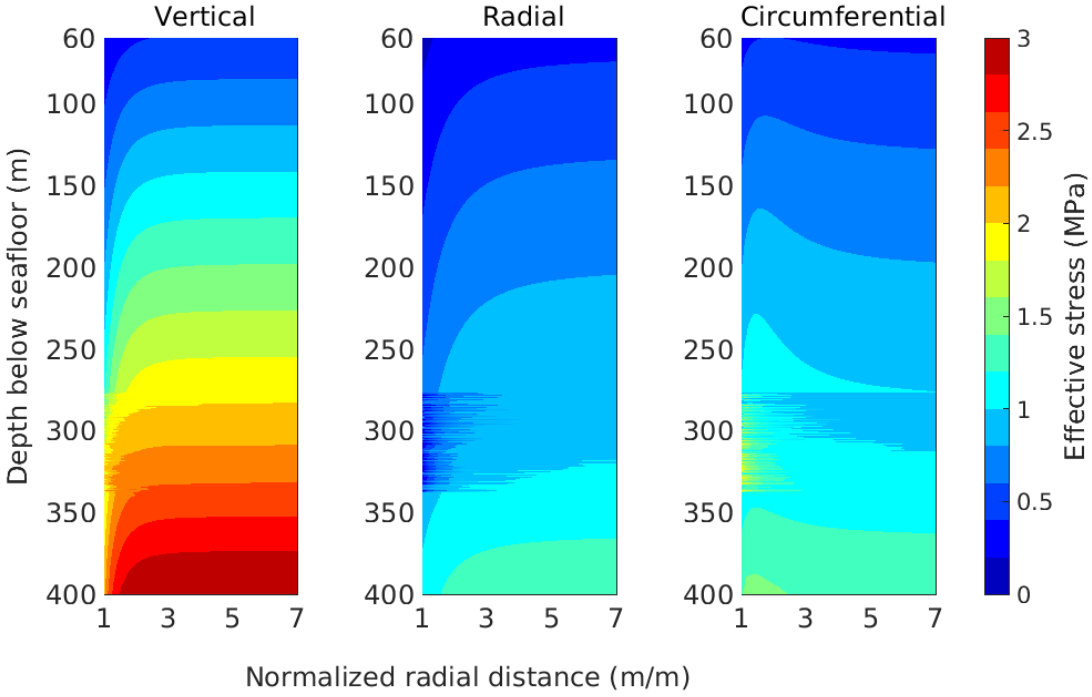
Vertical
Radial
Circumferential
Depth below seafloor (m)
60
100
150
200
250
300
350
400
1
3
5
7
Normalized radial distance (m/m)
Effective stress (MPa)
0
0.5
1
1.5
2
2.5
3

(a-2)

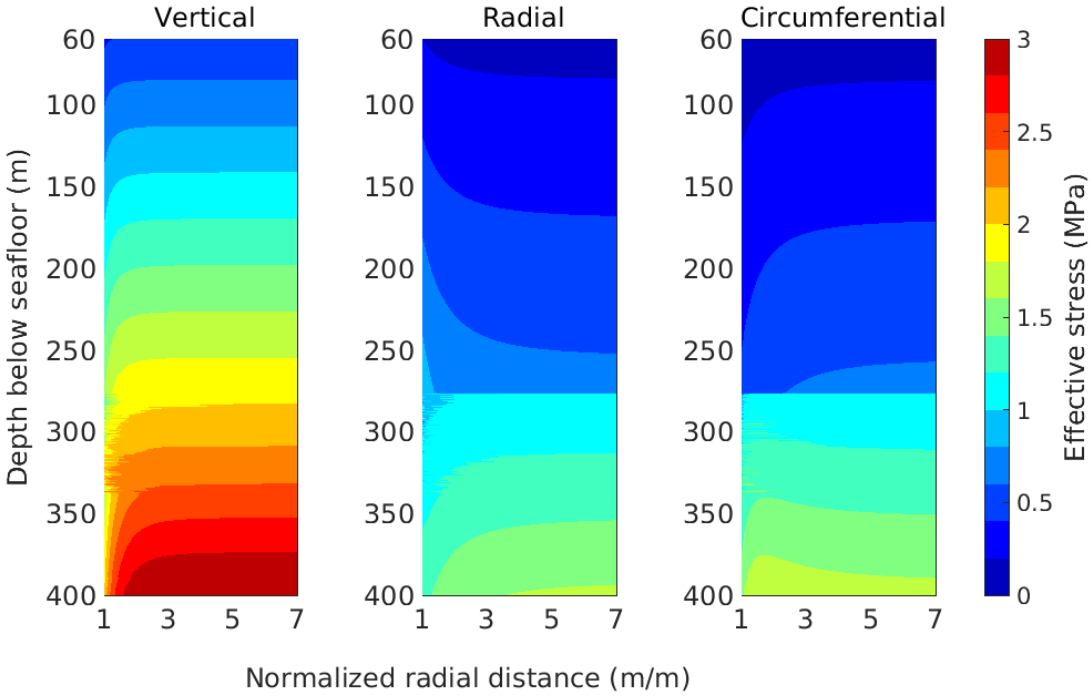
Vertical
Radial
Circumferential
Depth below seafloor (m)
60
100
150
200
250
300
350
400
1
3
5
7
Normalized radial distance (m/m)
Effective stress (MPa)
0
0.5
1
1.5
2
2.5
3

(b-1)

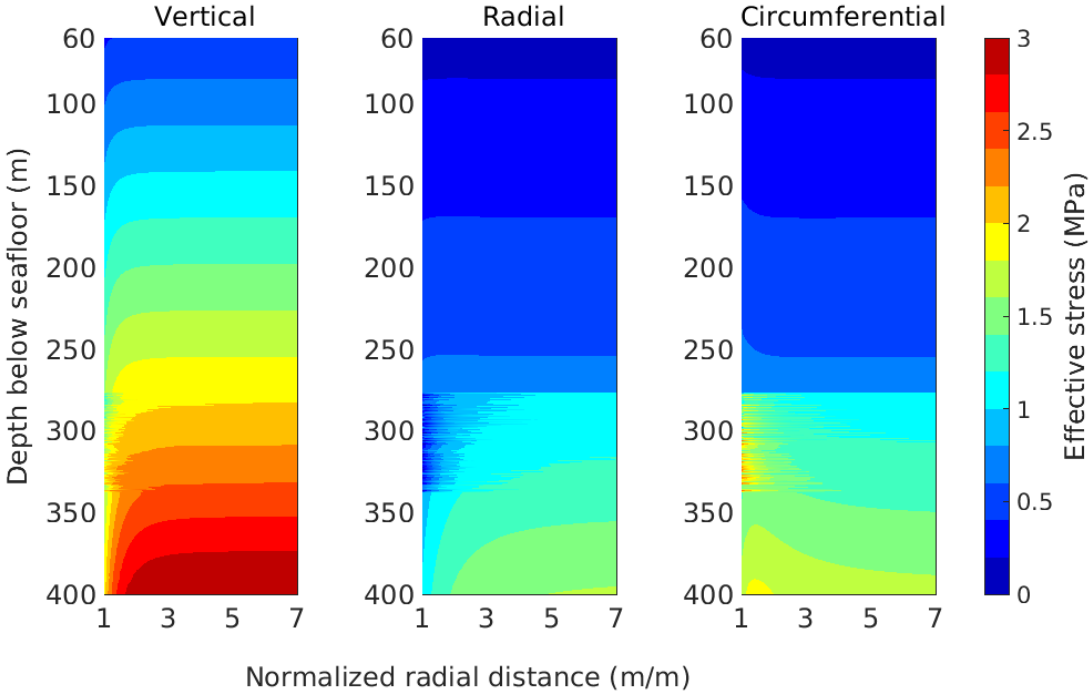
Vertical
Radial
Circumferential
Depth below seafloor (m)
60
100
150
200
250
300
350
400
1
3
5
7
Normalized radial distance (m/m)
Effective stress (MPa)
0
0.5
1
1.5
2
2.5
3

(b-2)

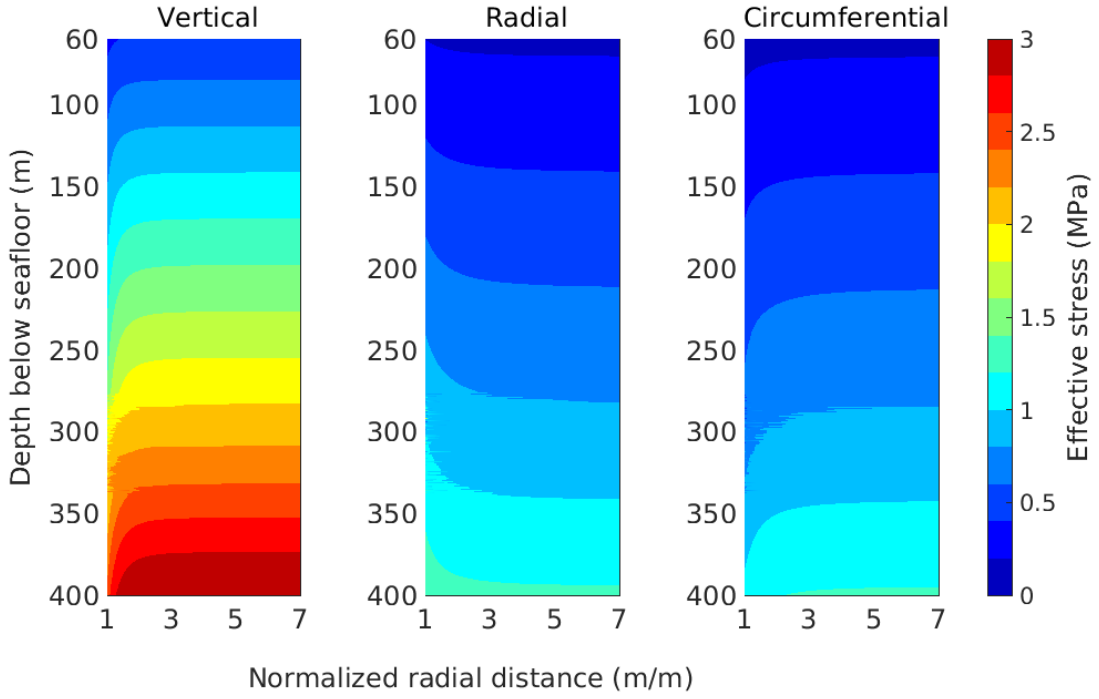

(c-1)

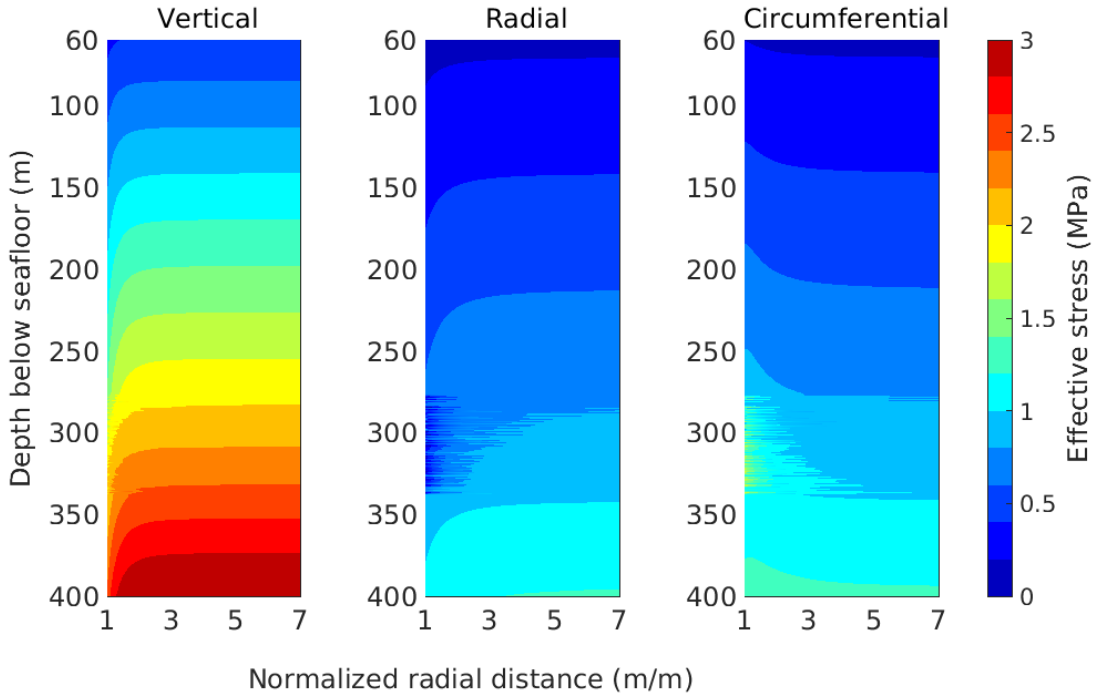

(c-2)

Figure 11 Effective stresses in the formation after the entire wellbore construction stages near the 12 1/4-in. diameter borehole: (a-1) $K_0 = (1-\sin\phi')\mathrm{OCR}^{\sin\phi'}$ with cement shrinkage = 0%; (a-2)

K_0 = (1-sinϕ')OCR$^{\sin\phi'}$ with cement shrinkage = 0.75%; (b-1) K_0 = ν/(1-ν) with cement shrinkage = 0%; (b-2) K_0 = ν/(1-ν) with cement shrinkage = 0.75%; (c-1) K_0 = 0.40 with cement shrinkage = 0%; (c-2) K_0 = 0.40 with cement shrinkage = 0.75%.

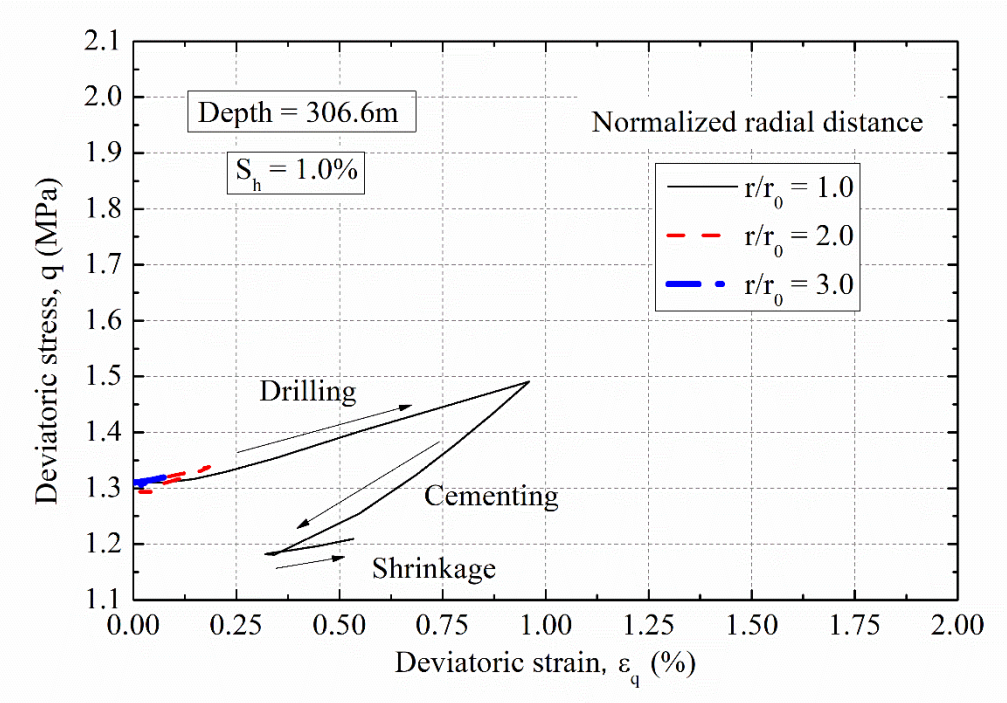

(a)

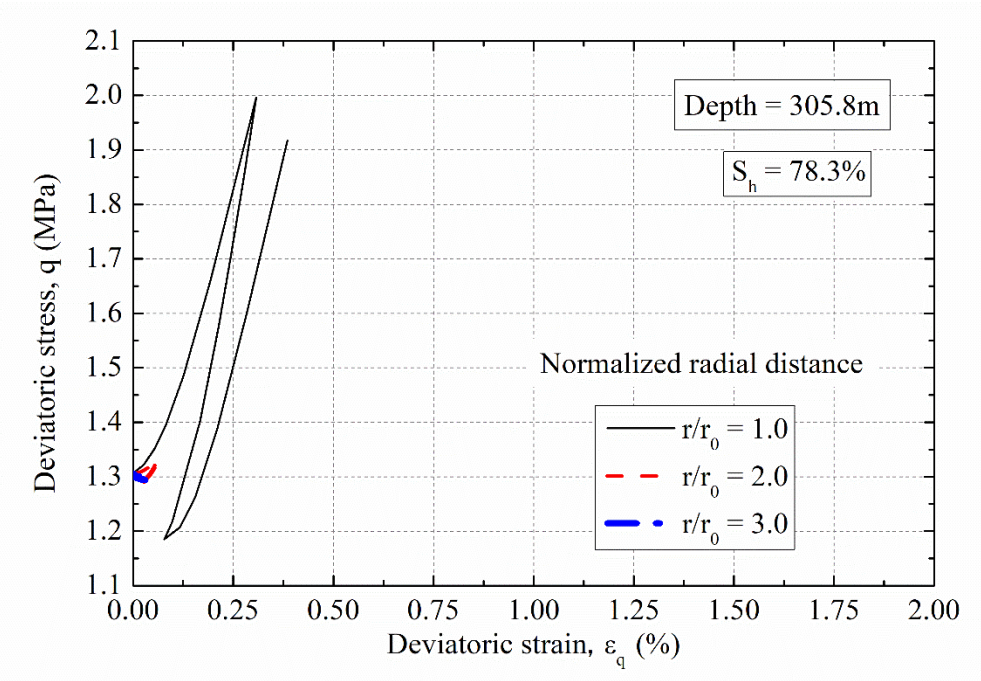

(b)

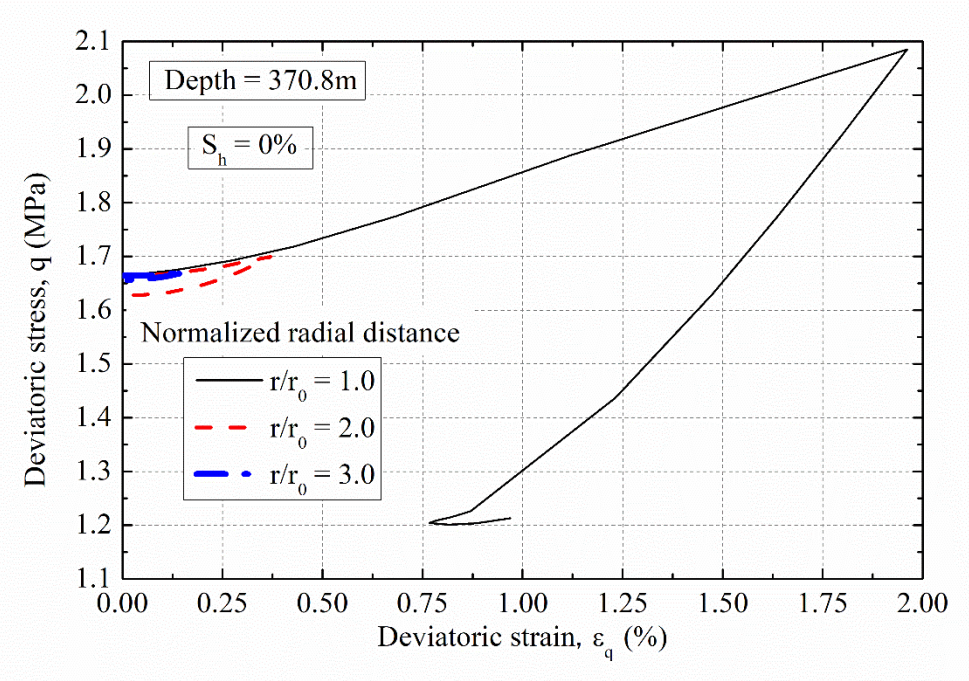

(c)

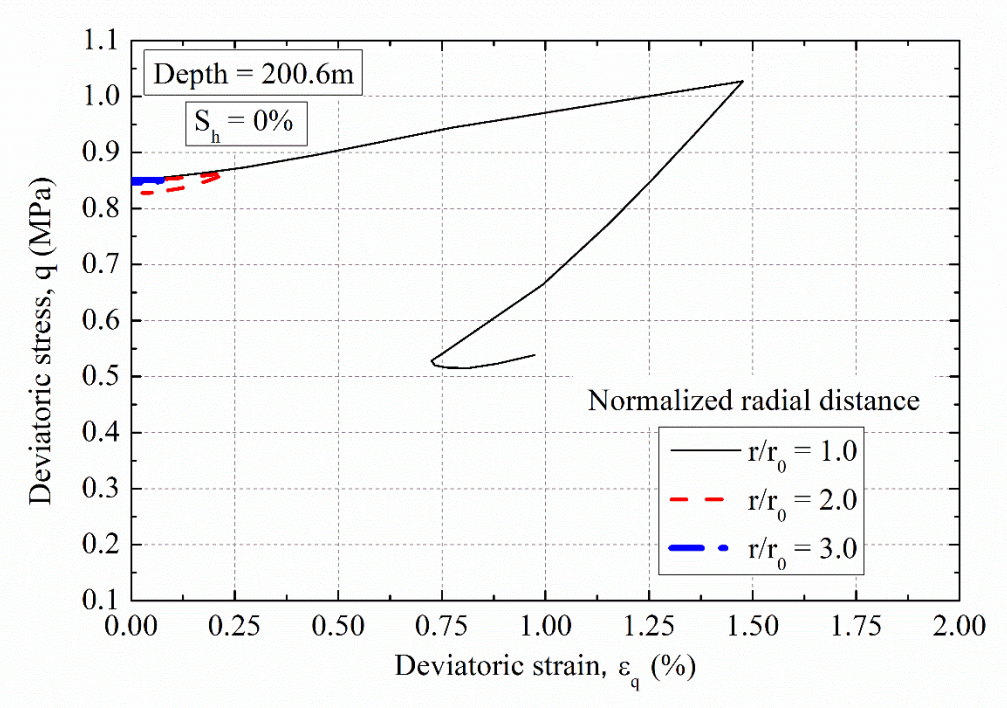

(d)

Figure 12 Deviatoric stress-strain changes of the formation (K_0 = 0.4) during well construction (cement shrinkage = 0.75%) at normalized radial distance of one, two and three: (a) methane hydrate reservoir (S_h = 1.0%); (b) methane hydrate reservoir (S_h = 78.3%); (c) underburden; (d) overburden.

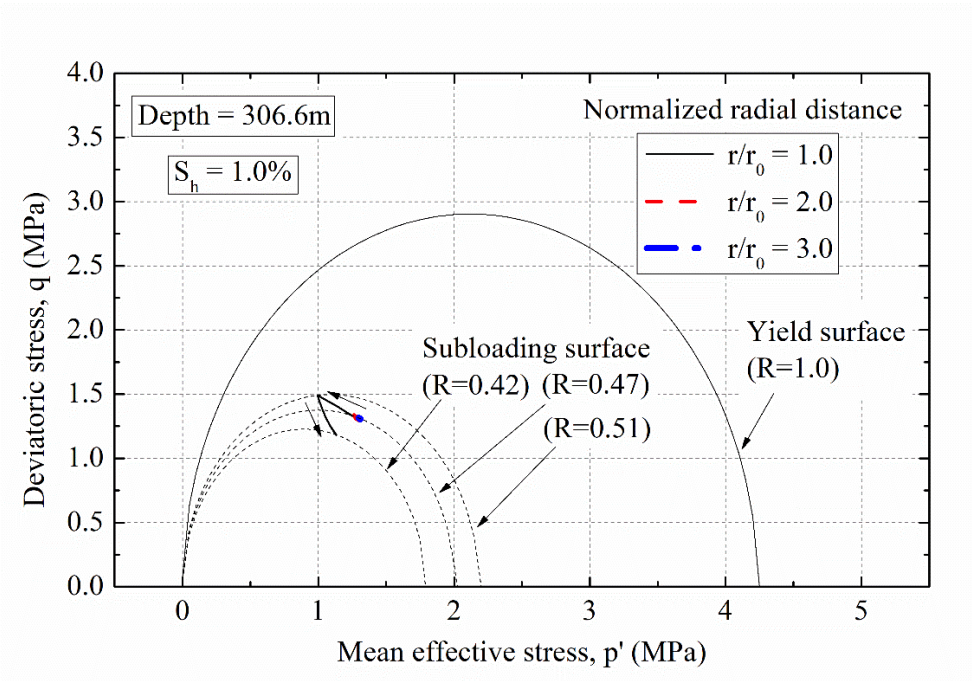
Depth = 306.6m
S_h = 1.0%
Normalized radial distance
r/r_0 = 1.0
r/r_0 = 2.0
r/r_0 = 3.0
Yield surface
(R=1.0)
Subloading surface
(R=0.42)
(R=0.47)
(R=0.51)
Deviatoric stress, q (MPa)
Mean effective stress, p' (MPa)
4.0
3.5
3.0
2.5
2.0
1.5
1.0
0.5
0.0
0
1
2
3
4
5

(a)

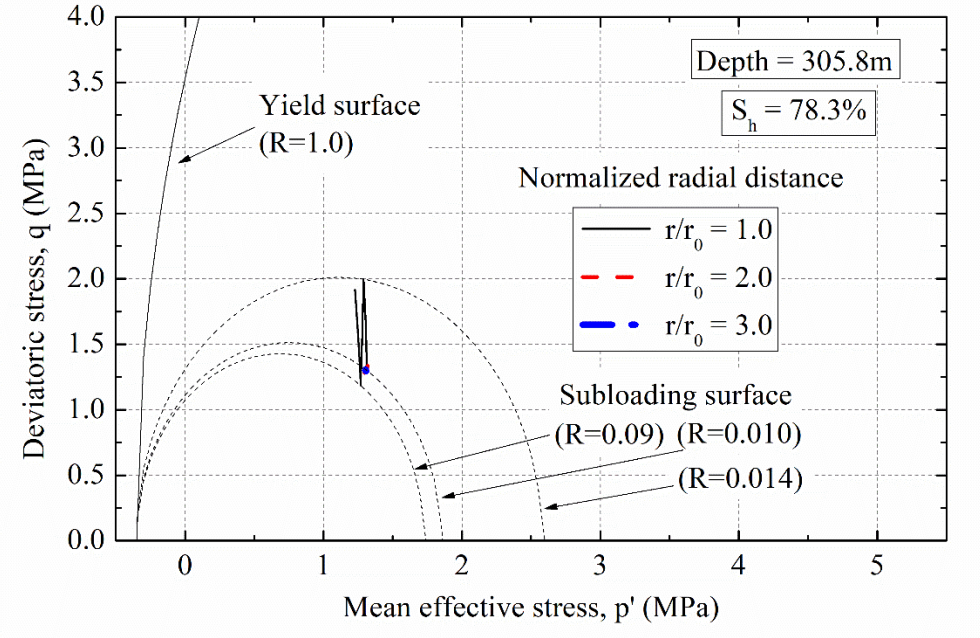
Depth = 305.8m
S_h = 78.3%
Yield surface
(R=1.0)
Normalized radial distance
r/r_0 = 1.0
r/r_0 = 2.0
r/r_0 = 3.0
Subloading surface
(R=0.09)
(R=0.010)
(R=0.014)
Deviatoric stress, q (MPa)
Mean effective stress, p' (MPa)
4.0
3.5
3.0
2.5
2.0
1.5
1.0
0.5
0.0
0
1
2
3
4
5

(b)

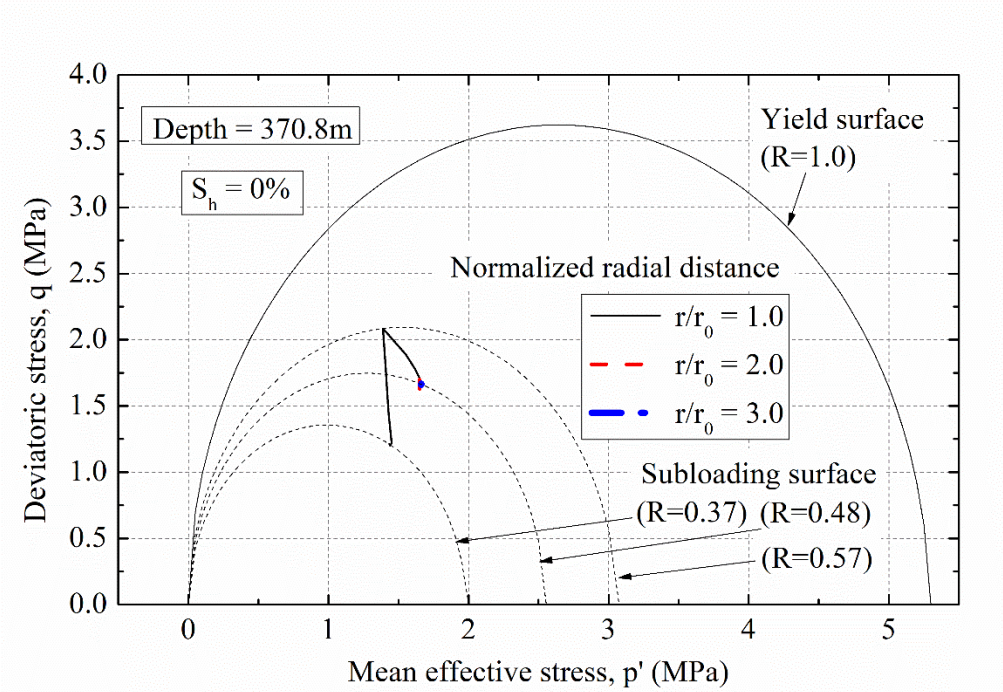

(c)

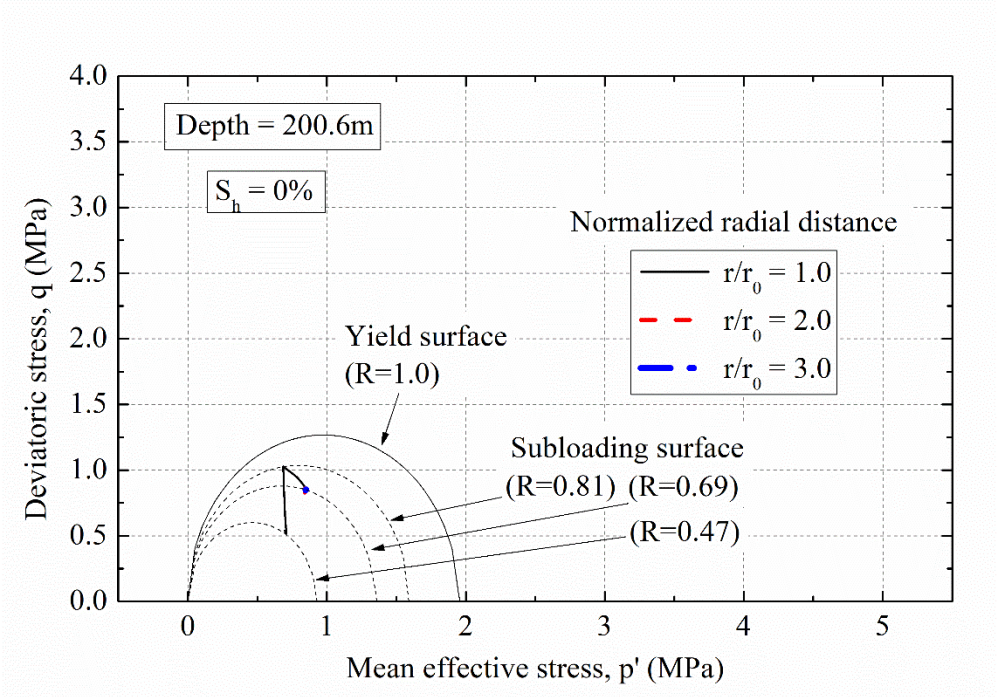

(d)

Figure 13 Deviatoric stress-mean effective stress changes (i.e. stress paths) of the formation (K_0 = 0.4) during well construction (cement shrinkage = 0.75%) at normalized radial distance of one, two and three: (a) methane hydrate reservoir (S_h = 1.0%); (b) methane hydrate reservoir (S_h = 78.3%); (c) underburden; (d) overburden. The oval semicircles are the MHCS subloading and

yield surfaces.

3.3. Zone of plastic deviatoric strain development in the formation

3.3.1. Effect of cement volume shrinkage

Figure 14 show the effect of cement shrinkage on the plastic deviatoric strain development in the formation near the 12 1/4-in. diameter borehole. Three cement volume shrinkage values (0%, 0.5% and 0.75%) are considered. The horizontal axis is the normalized radial distance, i.e., radial coordinates normalized by the radius of the 12 1/4-in. diameter borehole. The vertical coordinate covers the depths along the 12 1/4-in. diameter borehole. The initial horizontal stress was calculated by $K_0 = (1\text{-}\sin\phi')\mathrm{OCR}^{\sin\phi'}$.

Results show that the cement shrinkage stage would have minor effects on the plastic deviatoric strain development in the formation compared to the drilling stage, as the variation of cement shrinkage volume between 0% and 0.75% only slightly increased the area and magnitude of the plastic deviatoric strain in the formation. This is in contrast with the cement shrinkage-induced stress changes in the formation described in the previous section. The stress changes were caused by the stiffness contrast between the high hydrate saturation layers (elastic) and low/zero hydrate saturation layers (plastic) induced during the drilling stage. In other words, cement shrinkage converted the stiffness contrast into stress contrast without accumulating extra plastic strain. This is why the stress state was significantly affected by cement shrinkage whereas the plastic strain development was not influenced by it. The maximum magnitude of plastic deviatoric strain was approximately 1% at 60 m below seafloor in the clayey overburden layer. A comparable magnitude of plastic deviatoric strain was also developed in the sandy underburden layer. In the methane hydrate reservoir, however, the magnitude of plastic deviatoric strain was much smaller than in the overburden and underburden layers due to the reinforcement effect of methane hydrate.

The trend of plastic deviatoric strain development shown in Figure 14 could be related to the borehole radius measurement data obtained from wireline logging in the A1-W well (Figure 2). The radial extent of the computed deviatoric plastic strain is in agreement with the borehole radius data. The small deviatoric plastic strain levels in the methane hydrate reservoir (277 m-339 m) coincide with the minimal borehole enlargement, while the large plastic strain magnitudes in the overburden and underburden layers match well with the significant borehole enlargement. Although this qualitative comparison between the computed plastic strain distribution and measured borehole enlargement does not directly demonstrate the accuracy of the simulation, it indicates that the essential aspects of the formation behavior during well construction are captured in the constitutive model. It is noted that the A1-W well was dedicated for wireline logging to

probe formation properties, one of which was borehole radius, and was thus not constructed with casing and cement (Takahashi & Tsuji 2005). In fact, the A1-E1 well was the only vertical well that was constructed with casing and cement during the 2004 drilling campaign.

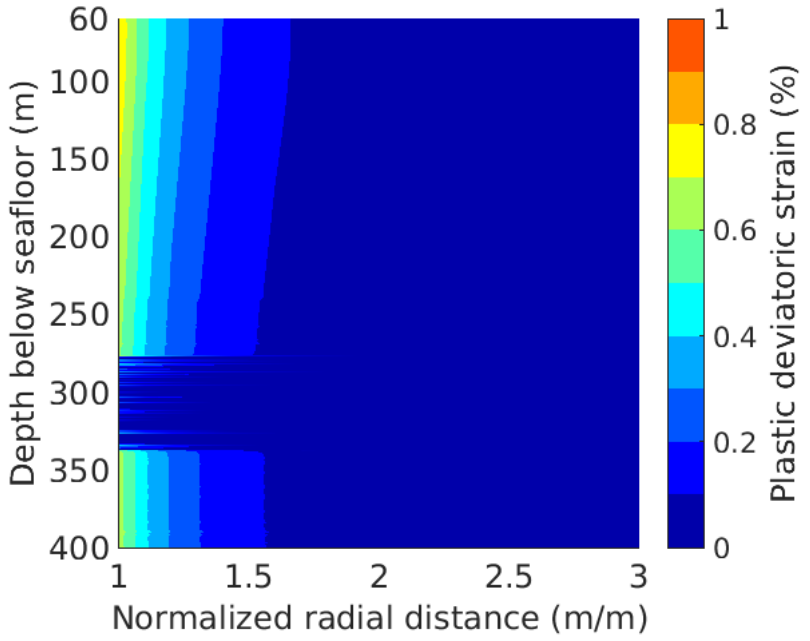

(a)

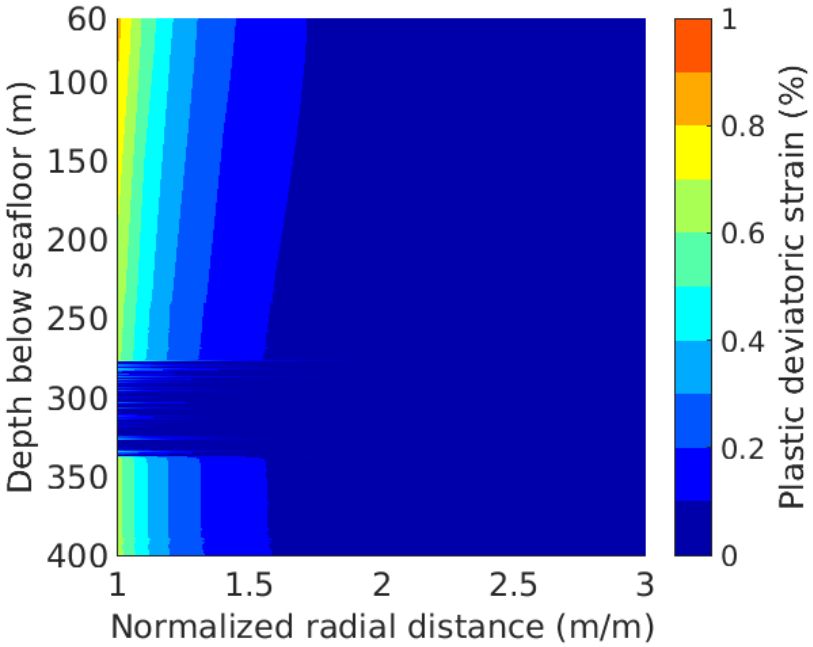

(b)

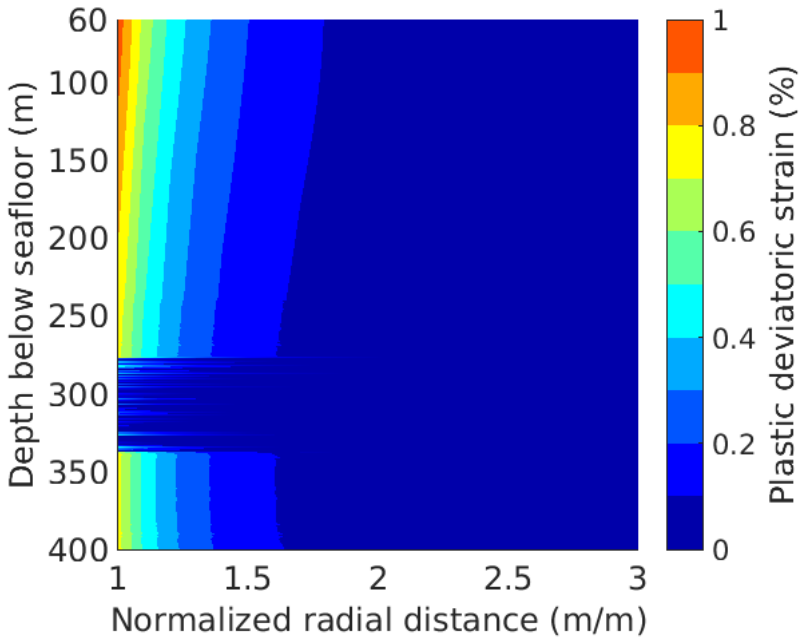

(c)

Figure 14 Effect of different volumes of cement shrinkage on the zone and magnitude of plastic deviatoric strain in the formation near the 12 1/4-in. diameter borehole: (a) cement shrinkage = 0%; (b) cement shrinkage = 0.5%; (c) cement shrinkage = 0.75%. The initial horizontal stress was calculated with $K_0 = (1\text{-}\sin\phi')\text{OCR}^{\sin\phi'}$.

3.3.2. Effect of initial horizontal stress of the formation

Figure 15 shows the effect of different initial horizontal stress formula on the plastic deviatoric strain development in the formation around the 12 1/4-in. diameter borehole. The initial horizontal stress of the formation was found to have an impact on the plastic deviatoric strain development compared to the effect of cement volume shrinkage discussed earlier. When $K_0 = (1\text{-}\sin\phi')\text{OCR}^{\sin\phi'}$ was employed, the maximum plastic deviatoric strain was developed at approximately 60m below seafloor in the overburden layer, while it was in the underburden layer when $K_0 = \nu/(1\text{-}\nu)$ was employed. When $K_0 = 0.40$ was used, the magnitude of the plastic deviatoric strain gradually increased with depth intermitted by the reservoir where the plasticity was minimal. The magnitude of plastic deviatoric strain can be related to the magnitude of initial horizontal effective stress. For instance, when $K_0 = \nu/(1\text{-}\nu)$ was employed, the largest initial horizonal effective stress occurred in the underburden layer. When $K_0 = 0.40$ was used, the initial horizontal effective stress linearly increased with depth. These trends of the initial horizontal effective stress corresponded well to those of the plastic deviatoric strain. This is because deviatoric stress development was proportional to the difference between the initial horizontal stress and drilling fluid (seawater) pressure (i.e., initial horizontal effective stress). The plastic deviatoric strain propagated to the

normalized radial distance of approximately one and a half among the examined simulation cases with different K_0 distributions.

Chen et al. (2018) showed that the change in hydrate saturation caused by well construction in the near-wellbore region would significantly affect the short-term gas production rate. The discrepancy between the simulation and field data on the short-term gas production rate at the Nankai Trough (Chen, Feng, Kogawa, et al. 2018) could also be due to well construction-induced complex initial permeability, gas and water saturation conditions around the wellbore prior to gas production. The result of this study on the plastic strain development in the methane hydrate-bearing layer in the near-wellbore region suggests that the effect of well construction-induced disturbance could indeed be complex yet limited within a very small radius from the center of the well. Therefore, the discrepancy between the predicted and actual short-term gas production rate might be due to other factors such as hydrate reformation during initial gas production.

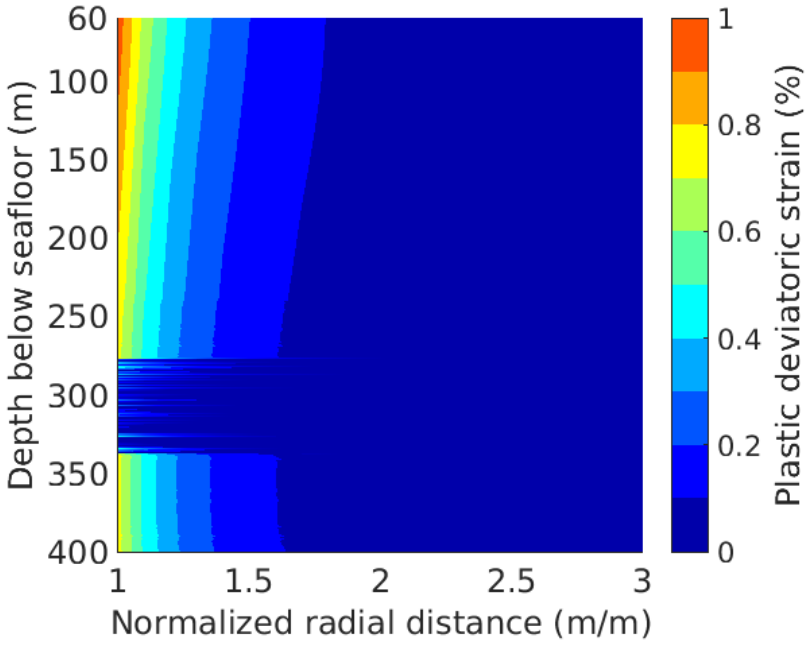

(a)

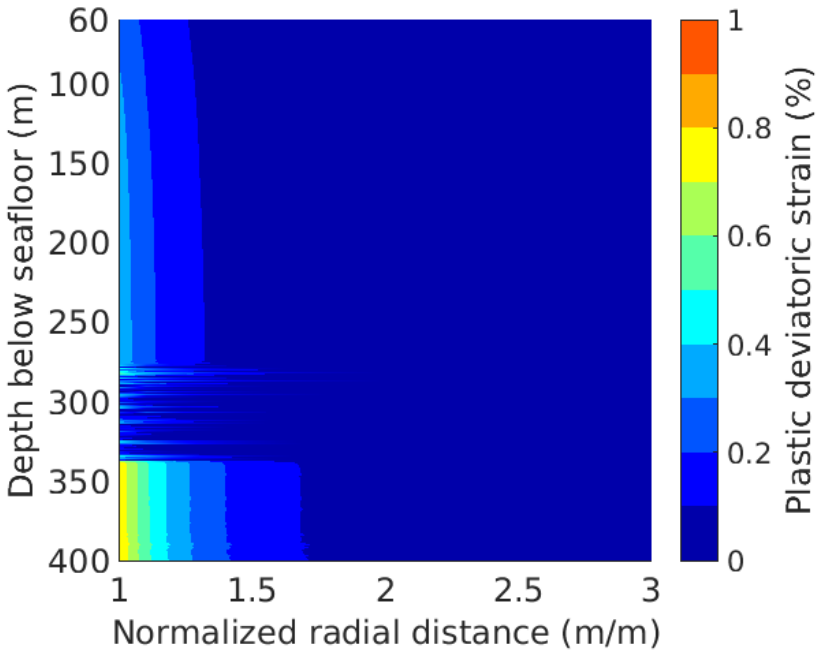

(b)

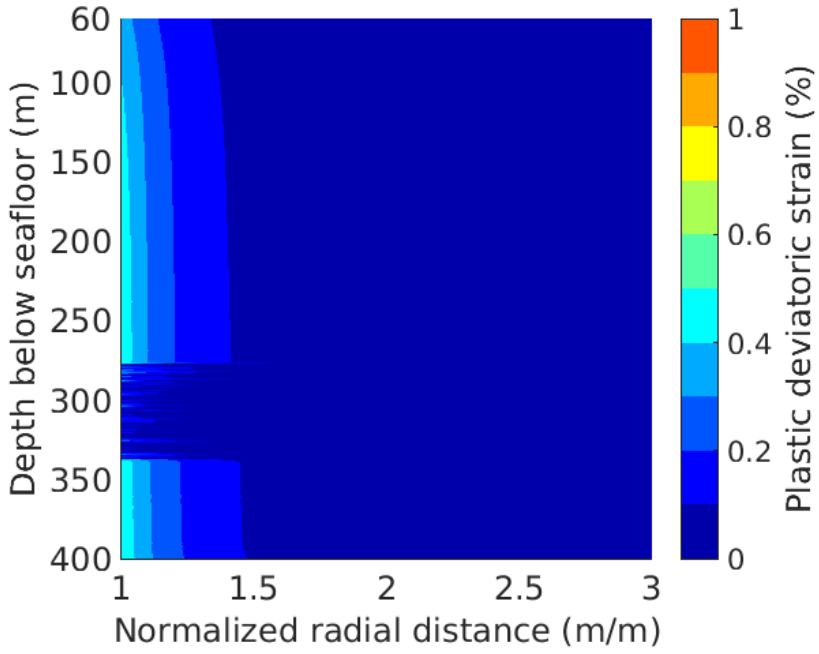

(c)

Figure 15 Effect of different initial horizontal stresses of the formation on the zone and magnitude of plastic deviatoric strain development in the formation near the 12 1/4-in. diameter borehole: (a) $K_0 = (1-\sin\phi')\mathrm{OCR}^{\sin\phi'}$; (b) $K_0 = \nu/(1-\nu)$; (c) $K_0 = 0.40$. The volume of cement shrinkage was set to 0.75%.

4. Conclusions

In this study, a modelling methodology of well construction process is proposed. The modelled well construction processes are drilling, casing hanging, cementing, cement hardening/shrinkage and casing landing. A finite element analysis incorporating this methodology was carried out to investigate the effect of wellbore construction on the integrity of the Nankai Trough unconsolidated methane hydrate-bearing formation. The effects of key well construction stages, including the drilling and cement volume shrinkage stage, as well as the effect of initial horizontal stress of the formation on the formation integrity were assessed. The primary findings from the present study are provided below.

(i) In the Nankai Trough methane hydrate reservoir case, the well construction-induced stress disturbance in the formation extended to the normalized radial distance of approximately three, whereas plastic deviatoric strain development extended to that of one and a half.

(ii) The high hydrate saturation layer in the reservoir remained elastic during the drilling stage due to the strength enhancement effect of the hydrate. In contrast, the low to zero hydrate saturation layer and the overburden/underburden layer developed plastic deformation. Because of the difference between the elastic (high) and plastic (low) stiffness, the high hydrate saturation layer exhibited larger stress changes in the subsequent well construction stages than the low to zero hydrate saturation layer and the overburden/underburden layer.

(iii) The key well construction process for estimating plastic strain development in the formation was found to be the drilling stage, whereas it was the cement shrinkage stage that was essential to predict formation stress changes.

From the above findings, it is recommended that the modelling of drilling stages should be sufficient if the focus of well construction modelling is to predict plastic strain development in the unconsolidated methane hydrate-bearing formation, whereas the modelling of cement shrinkage stages must also be incorporated if the estimation of formation stress changes is important. In addition, an appropriate initial horizontal stress distribution should be assigned to the formation as it has an impact on both stress changes and plastic strain development in the formation during well construction process.

Acknowledgements

The authors are grateful for the support provided by the MH21 Research Consortium, which facilitated the present research work. The triaxial test data on the formation samples were provided by Shimizu Corporation and the National Institute of Advanced Industrial Science and Technology (AIST). The well logging data were provided from Japan Oil, Gas and Metals National Corporation (JOGMEC). We sincerely appreciate their generosity. A special thanks goes to Koji Yamamoto at JOGMEC for providing fresh insights and continuous support for this research.

Appendices

Details of the methane hydrate critical state (MHCS) constitutive model (Uchida 2012; Uchida et al. 2012) are clarified herein. As the essential components of any constitutive models are (1) elastic properties, (2) yield criterion, (3) flow rule and (4) hardening rule (Wood 2004), each of these segments of the MHCS model are characterized below.

(1) Elastic properties

The isotropic elastic stiffness matrix of hydrate-bearing soil ($\boldsymbol{D}_{hs}^{e}$) is assumed to be comprised of that of soil skeleton and some contribution from hydrate. The effective stress vector ($\boldsymbol{\sigma'}$) is calculated from the reference stress vector ($\boldsymbol{\sigma}_0'$), the stiffness matrix of hydrate-bearing soil and elastic strain vector ($\boldsymbol{\epsilon}^{e}$) as follows:

$$\boldsymbol{\sigma'} - \boldsymbol{\sigma}_0' = \boldsymbol{D}_{hs}^{e}\boldsymbol{\epsilon}^{e} \tag{A-1}$$

The stress state of hydrate-bearing soil changes not only with elastic strain increments but also with hydrate dissociation-induced softening. This necessitates the incorporation of changes in the stiffness of hydrate-bearing soil due to hydrate dissociation ($d\boldsymbol{D}_{hs}^{e} = (\partial \boldsymbol{D}_{hs}^{e}/\partial S_h)dS_h$) in addition to the elastic strain increment ($d\boldsymbol{\epsilon}^{e}$), in order to calculate the increment of effective stress ($d\boldsymbol{\sigma'}$). Hence, the effective stress increment is calculated as follows:

$$d\boldsymbol{\sigma'} = \boldsymbol{D}_{hs}^{e} d\boldsymbol{\epsilon}^{e} + d\boldsymbol{D}_{hs}^{e}\boldsymbol{\epsilon}^{e} \tag{A-2}$$

The two elastic parameters for the isotropic elastic stiffness matrix of hydrate-bearing soil, namely the bulk modulus (K_{hs}) and shear modulus (G_{hs}), are calculated as follows:

$$K_{hs} = K_s + K_h \approx K_s = \frac{p'}{\kappa(1-n)} \tag{A-3}$$

$$G_{hs} = G_s + G_h = \frac{3(1-2\nu)}{2(1+\nu)} K_s + m_2 \chi S_h \tag{A-4}$$

Stiffness contribution of hydrate (K_h) to the bulk modulus of hydrate-bearing soil is assumed to be negligible compared to the bulk modulus of soil skeleton (K_s). The bulk modulus of soil skeleton is set dependent on the current value of the mean effective stress (p'). The κ parameter is the gradient of swelling line (Schofield & Wroth 1968) and n is porosity. The shear modulus of hydrate-bearing soil is computed as the summation of the shear modulus of soil skeleton (G_s) and that of hydrate (G_h). The former is calculated from the bulk modulus and Poisson's ratio (ν) of the soil skeleton while the latter is assumed to be proportional to hydrate saturation (S_h). The m_2 parameter is a constant while the χ parameter ranges from 1 (initial value) to 0 (ultimate value) depending on the accumulated plastic deviatoric strain which induces shear degradation of the stiffness contribution of hydrate.

(2) Yield criterion

The Hashiguchi subloading surface (Hashiguchi 1989) is incorporated in the MHCS model. The subloading surface is an auxiliary yield surface within the yield surface which is designed to produce small plastic strains prior to yielding. The subloading surface thus helps introduce smooth transition from elastic constitutive behaviors to plastic ones. A schematic diagram of an MHCS yield surface and subloading surfaces is shown in Figure A-1. The subloading surface of the MHCS model is defined as follows:

$$f(\boldsymbol{\sigma}', p'_{cs}, p'_{cd}, p'_{cc}, R) = q^2 + M^2(p' + p'_{cc})\big(p' - R(p'_{cs} + p'_{cd} + p'_{cc})\big) \tag{A-5}$$

where q ($= \sqrt{3J_2}$) = deviatoric stress (J_2= the second invariant of deviatoric stress tensor); p' ($= tr(\boldsymbol{\sigma}')/3$) = mean effective stress; M = critical state frictional constant; p'_{cs} = preconsolidation stress; p'_{cd} = dilation enhancement parameter; p'_{cc} = cohesion enhancement parameter; R = Hashiguchi subloading surface ratio. The yield surface is defined by the same equation ($R = 1$). The subloading surface ratio, R, can take a positive value up to 1 which indicates the separation between the subloading surface ($0 < R < 1$)) and yield surface ($R = 1$). The consistency condition is shown below:

$$df = \frac{\partial f}{\partial q} dq + \frac{\partial f}{\partial p'} dp' + \frac{\partial f}{\partial p'_{cs}} dp'_{cs} + \frac{\partial f}{\partial p'_{cd}} dp'_{cd} + \frac{\partial f}{\partial p'_{cc}} dp'_{cc} + \frac{\partial f}{\partial R} dR = 0 \tag{A-6}$$

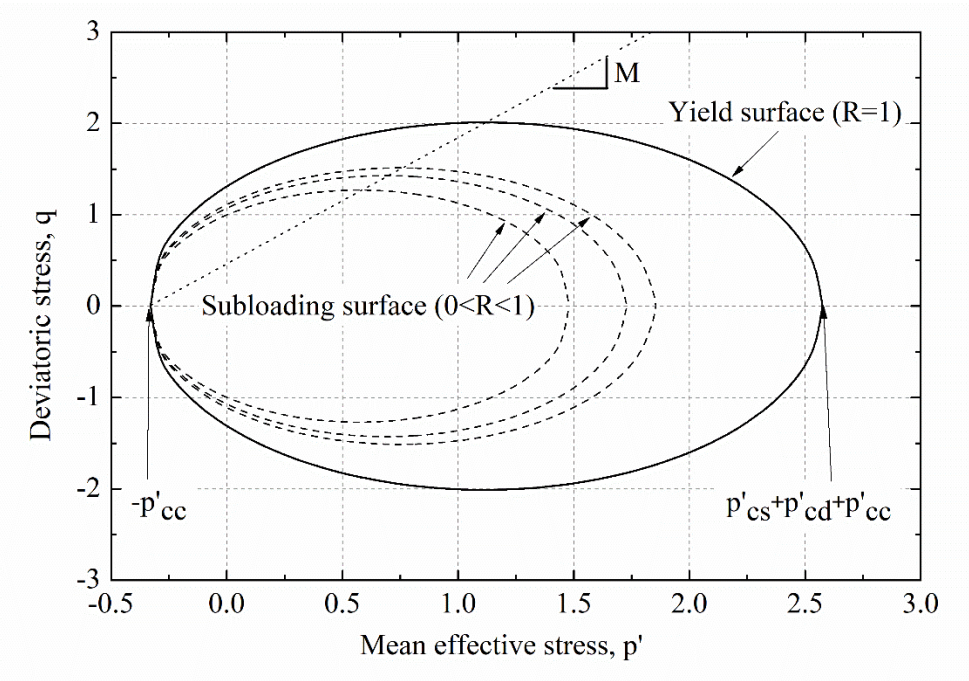

Figure A-1 A schematic diagram of an MHCS yield surface and subloading surfaces, which have a symmetric elliptic shape.

(3) Flow rule

Associated flow rule (i.e. plastic potential function (g) = yield criterion (f)) is employed in the MHCS model. Plastic strains are calculated with the plastic multiplier (λ) as follows:

$$d\boldsymbol{\epsilon}^p = \lambda \frac{\partial g}{\partial \boldsymbol{\sigma}'} = \lambda \frac{\partial f}{\partial \boldsymbol{\sigma}'} \tag{A-7}$$

(4) Hardening rule

There are four hardening parameters in the MHCS model ($p'_{cs},\ p'_{cd},\ p'_{cc},\ R$). Plastic volumetric hardening is employed for the preconsolidation stress (p'_{cs}) as follows:

$$dp'_{cs} = \frac{p'_{cs}}{(\lambda - \kappa)(1 - n)} d\epsilon_v^p \tag{A-8}$$

where λ, κ = the gradient of compression line and swelling line, respectively (Schofield & Wroth 1968); n = porosity; $d\epsilon_v^p$ = plastic volumetric strain increment. Plastic deviatoric hardening along with hydrate dissociation-induced hardening are employed for the dilation enhancement parameter (p'_{cd}) and cohesion enhancement parameter (p'_{cc}) as follows:

$$dp'_{cd} = ab(\chi S_h)^{b-1}\left(-m_1 \chi S_h d\epsilon_d^p + \chi dS_h\right) \tag{A-9}$$

$$dp'_{cc} = cd(\chi S_h)^{d-1}\left(-m_1 \chi S_h d\epsilon_d^p + \chi dS_h\right) \tag{A-10}$$

where a, b = constants for the dilation enhancement parameter; c, d = constants for the cohesion enhancement parameter; S_h = hydrate saturation; χ = a parameter for shear degradation of hydrate; m_1 = a constant for shear degradation of hydrate; $d\epsilon_d^p$ = plastic deviatoric strain increment. A combination of plastic volumetric and deviatoric hardening (the L^2 norm of plastic strain increments ($|d\epsilon^p|$)) is employed for the subloading surface ratio (R) with a constant (u) as shown in the equation below:

$$dR = -u\left(1 + \frac{p'_{cd} + p'_{cc}}{p'_{cs}}\right)\ln R\,|d\epsilon^p| \tag{A-11}$$

From the above equations, the plastic multiplier (λ) is calculated as below:

$$\lambda = \frac{\left(\frac{\partial f}{\partial \boldsymbol{\sigma}'}\right)^T \boldsymbol{D}_{hs}^e d\boldsymbol{\epsilon} + \left(\left(\frac{\partial f}{\partial \boldsymbol{\sigma}'}\right)^T \left(\frac{\partial \boldsymbol{D}_{hs}^e}{\partial S_h}\right)\boldsymbol{\epsilon}^e + \left(\frac{\partial f}{\partial S_h}\right)\right) dS_h}{\left(\frac{\partial f}{\partial \boldsymbol{\sigma}'}\right)^T \boldsymbol{D}_{hs}^e \left(\frac{\partial f}{\partial \boldsymbol{\sigma}'}\right) - \left(\frac{\partial f}{\partial \epsilon_v^p}\right)\left(\frac{\partial f}{\partial p'}\right) - \left(\frac{\partial f}{\partial \epsilon_d^p}\right)\left(\frac{\partial f}{\partial q}\right) - \left(\frac{\partial f}{\partial R}\frac{dR}{|d\boldsymbol{\epsilon}^p|}\right)\left|\frac{\partial f}{\partial \boldsymbol{\sigma}'}\right|} \tag{A-12}$$

Finally, the elastic-hardening plastic stress increment of the MHCS model is derived as shown below:

$$\begin{aligned} d\boldsymbol{\sigma}' &= \left(\boldsymbol{D}_{hs}^e - \frac{\boldsymbol{D}_{hs}^e \left(\frac{\partial f}{\partial \boldsymbol{\sigma}'}\right)\left(\frac{\partial f}{\partial \boldsymbol{\sigma}'}\right)^T \boldsymbol{D}_{hs}^e}{\left(\frac{\partial f}{\partial \boldsymbol{\sigma}'}\right)^T \boldsymbol{D}_{hs}^e \left(\frac{\partial f}{\partial \boldsymbol{\sigma}'}\right) - \left(\frac{\partial f}{\partial \epsilon_v^p}\frac{\partial f}{\partial p'}\right) - \left(\frac{\partial f}{\partial \epsilon_d^p}\frac{\partial f}{\partial q}\right) - \left(\frac{\partial f}{\partial R}\frac{dR}{|d\boldsymbol{\epsilon}^p|}\right)\left|\frac{\partial f}{\partial \boldsymbol{\sigma}'}\right|}\right) d\boldsymbol{\epsilon} \\ &+ \left(\left(\frac{\partial \boldsymbol{D}_{hs}^e}{\partial S_h}\right)\boldsymbol{\epsilon}^e - \frac{\boldsymbol{D}_{hs}^e \frac{\partial f}{\partial \boldsymbol{\sigma}'}\left(\left(\frac{\partial f}{\partial \boldsymbol{\sigma}'}\right)^T \left(\frac{\partial \boldsymbol{D}_{hs}^e}{\partial S_h}\right)\boldsymbol{\epsilon}^e + \left(\frac{\partial f}{\partial S_h}\right)\right)}{\left(\frac{\partial f}{\partial \boldsymbol{\sigma}'}\right)^T \boldsymbol{D}_{hs}^e \left(\frac{\partial f}{\partial \boldsymbol{\sigma}'}\right) - \left(\frac{\partial f}{\partial \epsilon_v^p}\frac{\partial f}{\partial p'}\right) - \left(\frac{\partial f}{\partial \epsilon_d^p}\frac{\partial f}{\partial q}\right) - \left(\frac{\partial f}{\partial R}\frac{dR}{|d\boldsymbol{\epsilon}^p|}\right)\left|\frac{\partial f}{\partial \boldsymbol{\sigma}'}\right|}\right) dS_h \end{aligned} \tag{A-13}$$

It is noted that terms for temperature and thermal strain are omitted in the above derivation of the

plastic multiplier and stress increment.

References

Appleby, S. & Wilson, A., 1996. Permeability and suction in setting cement. *Chemical Engineering Science*, 51(2), pp.251–267. https://doi.org/10.1016/0009-2509(95)00260-x.

Backe, K.R. et al., 1999. Characterizing Curing-Cement Slurries by Permeability, Tensile Strength, and Shrinkage. *SPE Drilling & Completion*, 14(3), pp.162–167. https://doi.org/10.2118/57712-PA.

Backe, K.R. et al., 1998. Shrinkage of Oil Well Cement Slurries. *The Journal of Cannadian Petroleum Technology*, 37(9), pp.63–67. https://doi.org/10.2118/98-09-06.

Bosma, M. et al., 1999. Design Approach to Sealant Selection for the Life of the Well. In *Proceedings of the 1999 SPE Annual Technical Conference and Exhibition*. Houston, Texas, pp. 1–14. https://doi.org/10.2523/56536-ms.

Boswell, R., 2013. Japan completes first offshore methane hydrate production test - methane successfully produced from deepwater hydrate layers. *Fire in the Ice*, 13(2). https://www.netl.doe.gov/research/oil-and-gas/methane-hydrates/fire-in-the-ice.

Chen, L., Feng, Y., Kogawa, T., et al., 2018. Construction and simulation of reservoir scale layered model for production and utilization of methane hydrate: The case of Nankai Trough Japan. *Energy*, 143, pp.128–140. https://doi.org/10.1016/j.energy.2017.10.108.

Chen, L., Feng, Y., Okajima, J., et al., 2018. Production behavior and numerical analysis for 2017 methane hydrate extraction test of Shenhu, South China Sea. *Journal of Natural Gas Science and Engineering*, 53(March), pp.55–66. https://doi.org/10.1016/j.jngse.2018.02.029.

Chenevert, M.E. & Jin, L., 1989. Model for Predicting Wellbore Pressures in Cement Columns. In *Proceedings of the 64th Annual Technical Conference and Exhibition of the Society of Petroleum Engineers*. San Antonio, Texas, pp. 35–47. https://doi.org/10.2118/spe-19521-ms.

Chenevert, M.E. & Shrestha, B.K., 1991. Chemical Shrinkage Properties of Oilfield Cements. *SPE Drilling Engineering*, 6(1), pp.37–43. Available at: https://doi.org/16654-PA.

Chenevert, M.E. & Shrestha, B.K., 1987. Shrinkage Properties of Cement. In *Proceedings of the 62nd Annual Technical Conference and Exhibition of the Society of Petroleum Engineers*. Dallas, Texas, pp. 49–57. https://doi.org/10.2118/16654-MS.

Goboncan, V.C. & Dillenbeck, R.L., 2003. Real-Time Cement Expansion / Shrinkage Testing Under Downhole Conditions For Enhanced Annular Isolation. In *Proceedings of the SPE/IADC Drilling Conference*. Amsterdam, The Netherlands, pp. 1–9. https://doi.org/10.2118/79911-ms.

Gray, K.E. et al., 2007. Finite Element Studies of Near-Wellbore Region During Cementing Operations : Part I. In *Proceedings of the SPE Production and Operations Symposium*. Oklahoma City, Oklahoma, pp. 1–15. https://doi.org/10.2118/106998-MS.

Hashiguchi, K., 1989. Subloading surface model in unconventional plasticity. *International Journal of Solids and Structures*, 25(8), pp.917–945. https://doi.org/10.1016/0020-7683(89)90038-3.

Hyodo, M. et al., 2014. Effects of dissociation on the shear strength and deformation behavior of methane hydrate-bearing sediments. *Marine and Petroleum Geology*, 51, pp.52–62. https://doi.org/10.1016/j.marpetgeo.2013.11.015.

Hyodo, M. et al., 2013. Mechanical and dissociation properties of methane hydrate-bearing sand in deep seabed. *Soils and Foundations*, 53(2), pp.299–314. https://doi.org/10.1016/j.sandf.2013.02.010.

Justnes, H. et al., 1995. Chemical shrinkage of oil well cement slurries. *Advance in Cement Research*, 7(26), pp.85–90. https://doi.org/10.1680/adcr.1995.7.26.85.

Kakumoto, M. et al., 2012. Frictional Strength between Casing and Cement under Confining Pressure. In *Proceedings of the Twenty-second (2012) International Offshore and Polar Engineering Conference*. Rhodes, Greece, pp. 77–82. https://www.onepetro.org/conference-paper/ISOPE-I-12-043.

Masui, A. et al., 2005. Effects of Methane Hydrate Formation on Shear Strength of Synthetic Methane Hydrate Sediments. In *Proceedings of the Fifteenth International Offshore and Polar Engineering Conference*. Seoul, South Korea, pp. 364–369. https://www.onepetro.org/conference-paper/ISOPE-I-05-056.

Masui, A. et al., 2007. Mechanical Properties of Sandy Sediment Containing Marine Gas Hydrates in Deep Sea Offshore Japan. In *Proceedings of the Seventh (2007) ISOPE Ocean Mining Symposium*. Lisbon, Portugal, pp. 53–56. https://www.onepetro.org/conference-paper/ISOPE-M-07-015.

Matsuzawa, M., Umezu, S. & Yamamoto, K., 2006. Evaluation of experiment program 2004: Natural hydrate exploration campaign in the Nankai-Trough offshore Japan. *SPE/IADC Drilling Conference, Proceedings*, pp.511–523. https://doi.org/10.2523/98960.

Miyazaki, K. et al., 2011. Triaxial compressive properties of artificial methane-hydrate-bearing sediment. *Journal of Geophysical Research: Solid Earth*, 116, pp.1–11. https://doi.org/10.1029/2010jb008049.

Miyazaki, K. et al., 2007. Variable-Compliance-Type Constitutive Model for Toyoura Sand Containing Methane Hydrate. In *Proceedings of the Seventh (2007) ISOPE Ocean Mining Symposium*. Lisbon, Portugal, pp. 57–62. https://www.onepetro.org/conference-paper/ISOPE-M-07-017.

Nagano, Y., Lin, W. & Yamamoto, K., 2015. In-situ stress analysis using the anelastic strain recovery (ASR) method at the first offshore gas production test site in the eastern Nankai Trough, Japan. *Marine and Petroleum Geology*, 66, pp.418–424. https://doi.org/10.1016/j.marpetgeo.2015.02.027.

Nishio, S., Ogisako, E. & Denda, A., 2011. Geotechnical Properties of Seabed Ground in East Nankai Trough. In *Proceedings of the 7th International Conference on Gas Hydrates (ICGH 2011)*. Edinburgh, Scotland, United Kingdom. https://doi.org/10.5026/jgeography.118.955.

Oyarhossein, M. & Dusseault, M.B., 2015. Wellbore Stress Changes and Microannulus Development Because of Cement Shrinkage. In *Proceedings of the 49th US Rock Mechanics / Geomechanics Symposium*. San Francisco, CA, USA. https://www.onepetro.org/conference-paper/ARMA-2015-118.

Ravi, K., Bosma, M. & Gastebled, O., 2002. Safe and Economic Gas Wells through Cement Design for Life of the Well. In *Proceedings of the SPE Gas Technology Symposium*. Calgary, Alberta, Canada, pp. 1–15. https://doi.org/10.2523/75700-ms.

Reddy, B. et al., 2009. Cement-Shrinkage Measurement in Oilwell Cementing--A Comparative Study of Laboratory Methods and Procedures. *SPE Drilling & Completion*, 24(1), pp.104–114. https://doi.org/10.2118/103610-PA.

Roscoe, K.H. & Burland, J.B., 1968. *On the Generalized Stress-Strain Behavior of 'Wet' Clay*, Cambridge, U. K.: Cambridge Univ. Press.

Sasaki, T., Soga, K. & Abuhaikal, M., 2018. Water absorption and shrinkage behaviour of early-age cement in wellbore annulus. *Journal of Petroleum Science and Engineering*, 169(March), pp.205–219. https://doi.org/10.1016/j.petrol.2018.05.065.

Schofield, A.N. & Wroth, C.P., 1968. *Critical State Soil Mechanics*, http://www-civ.eng.cam.ac.uk/geotech_new/publications/schofield_wroth_1968.pdf.

Shute, D.M., Kaiser, T.M.V. & Munoz, H., 2004. Compaction resistant wellbore for sand-producing wells. In *Canadian International Petroleum Conference*. pp. 1–8. https://doi.org/10.2118/2004-279.

Suzuki, K., Takayama, T. & Fujii, T., 2015. Density structure report from logging-while-drilling data and core data at the first offshore gas production test site on Daini-Atsumi Knoll around eastern Nankai Trough. *Marine and Petroleum Geology*, 66, pp.388–395. https://doi.org/10.1016/j.marpetgeo.2015.02.026.

Takahashi, H. & Tsuji, Y., 2005. Multi-Well Exploration Program in 2004 for Natural Hydrate in the Nankai-Trough Offshore Japan. In *Proceedings of the 2005 Offshore Technology Conference*. Houston, Texas, pp. 1–10. https://www.onepetro.org/conference-paper/OTC-17162-MS.

Thiercelin, M., Baumgarte, C. & Guillot, D., 1998. A Soil Mechanics Approach To Predict Cement Sheath Behavior. In *Proceedings of the SPE/ISRM Eurock '98*. Trondheim, Norway, pp. 329–337. https://doi.org/10.2118/14375-MS.

Uchida, S., 2012. *Numerical investigation of geomechanical behaviour of hydrate-bearing sediments*, Ph.D. thesis, University of Cambridge.

Uchida, S., Soga, K. & Yamamoto, K., 2012. Critical state soil constitutive model for methane hydrate soil. *Journal of Geophysical Research: Solid Earth*, 117, pp.1–13. https://doi.org/10.1029/2011jb008661.

Veeken, C.A.M., Wahleitner, J.P. & Keedy, C.R., 1994. Experimental modelling of casing deformation in a compacting reservoir. In *Proceedings of the 1994 Eurock SPE/ISRM Rock Mechanics in Petroleum Engineering Conference*. Delft, The Netherlands, pp. 497–506. https://doi.org/10.2523/28090-ms.

Wood, D.M., 2004. *Geotechnical Modelling*, Abingdon on Themes, Oxfordshire: Spon Press.

Xu, E., 2014. *Numerical Analysis of Wellbore Behaviour during Methane Gas Recovery from Hydrate Bearing Sediments*, Ph.D. thesis, University of Cambridge.

Yamamoto, K. et al., 2005. Application of Wireline Conveyed Through Casing Formation Tester to Methane Hydrate Research in Japan. In *Proceedings of the 11th Formation Evaluation Symposium of Japan*. pp. 1–12. https://ci.nii.ac.jp/naid/10025875980/.

Yamamoto, K. et al., 2006. Geomechanics data acquisition techniques used in the METI Tokai-oki to Kumano-nada drilling campaign. In *Proceedings of the 12th Formation Evaluation Symposium of Japan*. pp. 1–6.

Yamamoto, K. et al., 2014. Operational overview of the first offshore production test of methane hy- drates in the Eastern Nankai Trough. In *Proceedings of theOffshore Technology Conference*. Houston, Texas. https://doi.org/10.4043/25243-MS.

Yamamoto, K., 2015. Overview and introduction: Pressure core-sampling and analyses in the 2012-2013 MH21 offshore test of gas production from methane hydrates in the eastern Nankai Trough. *Marine and Petroleum Geology*. https://doi.org/10.1016/j.marpetgeo.2015.02.024.

Yamamoto, K. & Dallimore, S.R., 2008. Aurora-JOGMEC-NRCan Mallik 2006-2008 gas hydrate research project progress. *Fire in the Ice*, pp.1–5. https://www.netl.doe.gov/research/oil-and-gas/methane-hydrates/fire-in-the-ice.

Yoneda, J. et al., 2014. Evaluation of Frictional Properties for Methane-Hydrate-Well Completion and Production. *SPE Drilling & Completion*, March, pp.115–124. https://www.onepetro.org/journal-paper/SPE-169897-PA.

Yoneda, J. et al., 2015. Mechanical properties of hydrate-bearing turbidite reservoir in the first gas production test site of the Eastern Nankai Trough. *Marine and Petroleum Geology*, 66,

pp.471–486. https://doi.org/10.1016/j.marpetgeo.2015.02.029.

Zhou, D. & Wojtanowicz, A.K., 2000. New Model of Pressure Reduction to Annulus During Primary Cementing. In *Proceedings of the 2000 IADC/SPE Drilling Conference*. New Orleans, Louisiana, pp. 1–10. https://www.onepetro.org/conference-paper/SPE-59137-MS.